

¹ **Copyright**
² **by**
³ **Ryan Patrick Hannigan**
⁴ **2023**

5 The Dissertation Committee for Ryan Patrick Hannigan certifies that
6 this is the approved version of the following dissertation:

7 Stranger Things at the LHC

Committee:

Christina Markert, Supervisor

Peter Onyisi

Aaron Zimmerman

Chandrajit Bajaj

8

9

Stranger Things at the LHC

10

by

11

Ryan Patrick Hannigan, Ph.D.

12

Dissertation

13

Presented to the Faculty of the Graduate School of

14

The University of Texas at Austin

15

in Partial Fulfillment

16

of the Requirements

17

for the degree of

18

Doctor of Philosophy

19

The University of Texas at Austin

20

May, 2023

To Jaynee.

Chapter One: Introduction

23 The initial section of this chapter will mostly serve as a historical overview of the
24 field of particle physics, leading to the development of the **Standard Model**: the
25 theory that describes all of the fundamental¹ particles and the way in which they
26 interact with each other. An emphasis will be made on the discovery of quarks and
27 gluons, as the research presented in this thesis is centered around these particles.
28 The second section will more thoroughly introduce the Standard Model and its three
29 distinct sectors, with the goal to provide a high-level mathematical overview of the
30 theory.

31 The third section of this chapter will delve into the details of Quantum Chromo-
32 Dynamics (QCD), which is the component of the Standard Model that describes the
33 interactions between **quarks** and **gluons**, the constituent particles of the more famil-
34 iar protons and neutrons. As many theoretical calculations are difficult to perform
35 in QCD, the use of computationally-intensive numerical techniques is often required
36 to make precise predictions. One such prediction is a phase transition from nuclear
37 matter at everyday energies—in which the quarks and gluons are confined within
38 protons and neutrons—into a novel state of matter at extreme temperatures or den-
39 sities, known as the **Quark-Gluon Plasma** (QGP). Section 1.4 will detail the QGP
40 and many of its interesting properties predicted by QCD, with an emphasis on the
41 production of strange quarks within the plasma.

42 The final two sections of this chapter will discuss how high-energy particle col-
43 lisions can be used to study the QGP, using both expensive particle accelerators
44 (Section ??) and simulation techniques (Section 1.7).

¹As of the year 2023, but reading this chapter will hopefully illustrate why this may be subject to change in the (likely very distant) future.

45 1.1 What is fundamental?

46 The answer to the question

47 What are the fundamental building blocks of our universe?

48 has changed drastically over the course of human history. The idea that all matter
49 is composed of smaller, uncuttable pieces has been around since 5th century BCE
50 when Greek philosophers Democritus and Leucippus first introduced the concept of
51 an atom [1]. While this idea was mostly motivated by philosophical reasoning, it was
52 later adopted by the English scientist John Dalton in the 19th century to explain the
53 results of his chemical experiments, where he found that chemical elements always
54 combined with each other by discrete units of mass [2]. As scientists discovered more
55 and more of these elements, the number of “fundamental” building blocks grew as
56 well. By the late 1800s, over 70 unique chemical elements had been discovered, though
57 they would often be grouped together due to similar chemical properties using what
58 chemist Dimitri Mendeleev dubbed the *periodic table of elements* [3]. An example of
59 the periodic table from the time of Mendeleev can be seen in Figure 1.1. While this
60 grouping was useful for chemists, it also served as a hint to physicists that perhaps
61 these elements were not actually fundamental, but rather composed of even smaller
62 pieces.

H = 1	Ti = 50	Zr = 90	? = 180
Be = 9,4	V = 51	Nb = 94	Ta = 182
B = 11	Cr = 52	Mo = 96	W = 186
C = 12	Mn = 55	Rh = 104,4	Pt = 197,4
N = 14	Fe = 56	Ru = 104,4	Ir = 198
O = 16	Ni = Co = 59	Pd = 106,6	Os = 199
F = 19	Cu = 63,4	Ag = 108	Hg = 200
Li = 7 Na = 23	Zn = 65,2	Cd = 112	
	Al = 27,4	? = 68	Uu = 197?
	Si = 28	? = 70	Sn = 118
	P = 31	As = 75	Sb = 122
	S = 32	Se = 79,4	Te = 128?
	Cl = 35,5	Br = 80	J = 127
	K = 39	Rb = 85,4	Cs = 133
	Ca = 40	Sr = 87,6	Tl = 204
	? = 45	Ce = 92	Pb = 207
	?Er = 56	La = 94	
	?Yt = 60	Di = 95	
	?In = 75,6	Th = 118?	

Figure 1.1: Dimitri Mendeleev’s periodic table of elements from the late 1800s, taken from [4]. The elements are grouped by similar chemical properties, and the gaps in the table are where Mendeleev predicted that new elements would be discovered.

63 Scientists' understanding of the building blocks of matter changed again around
64 the turn of the 20th century, with physicists J.J. Thomson, Ernest Rutherford, and
65 James Chadwick determining that the supposedly indivisible atom was composed
66 of even smaller subatomic particles, eventually named electrons, protons, and neu-
67 trons [5]–[7]. Thus the number of fundamental blocks of matter had decreased sub-
68 stantially from nearly 100 to just three. However, this number would need to be
69 updated again only months later, as the fundamental anti-particle of the electron—
70 known as the positron—was discovered in 1932 by Carl Anderson [8]. In the next two
71 decades, the number of known fundamental particles would skyrocket. In 1947, the
72 muon was discovered [9], followed by the discovery of a laundry list of particles [10]–
73 [12] that participate in the same interaction that holds the positively charged protons
74 together in the nucleus of an atom—the so-called **strong nuclear force**. These “fun-
75 damental” particles were collectively called **hadrons**, which were further separated
76 into lighter and heavier categories, dubbed **mesons** and **baryons**, respectively [13].
77 By the late 1960s, the number of known hadrons had grown to well over 100 [14],
78 even more than the number of “fundamental” chemical elements that were known to
79 exist in the 1800s.

80 In the same way that Mendeleev tried to group the elements by their similar
81 chemical properties, physicists attempted to group the hadrons together based on
82 their known subatomic properties. The first successful attempt at such a grouping
83 was the **Eightfold Way**, which was independently proposed by Murray Gell-Mann
84 and Yuval Ne’eman in 1961 [15], [16]. This grouping was found by examining the
85 following properties of the hadrons:

- 86 1. **Isotopic spin:** a quantum number introduced by Werner Heisenberg in 1932
87 to try to explain the apparent symmetries between the proton and neutron
88 with respect to the strong nuclear force [17] (i.e. although the proton and
89 neutron have different electric charges, the strong interaction does not seem to
90 distinguish between the two)
- 91 2. **Strangeness:** another quantum number introduced by Gell-Mann and Nishi-
92 jima in 1953 to explain why some hadrons decayed much more slowly than
93 expected, and such particles appeared to be created in pairs [18]. In other
94 words, the strong interaction responsible for the creation of these particles ap-
95 peared to conserve this quantum number, but the weak interaction responsible

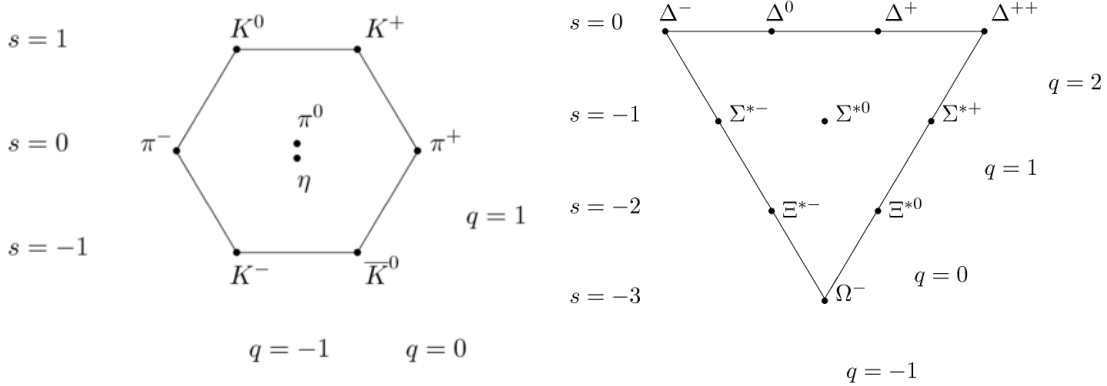


Figure 1.2: The “Eightfold Way” diagrams of the $J = 1/2$ mesons (left) and $J = 3/2$ baryons (right) plotted against strangeness and electric charge. Understanding the underlying symmetry group that gives rise to such patterns³ ultimately led to the development of the quark model. While the original patterns were found using isotopic spin and hypercharge, it is trivial to convert between the two using the Gell-Mann-Nishijima formula [19], [20].

96 for the slower decay of these particles did not. Strangeness² will be discussed
 97 in more detail in Section 1.3.2.4.

98 Plotting the baryons and mesons in a two-dimensional space based on these two
 99 properties revealed striking patterns, as shown in Figure 1.2. Similar to Mendeleev,
 100 GellMann also left a blank space⁴ where he believed a new particle—the Ω^- —would
 101 be discovered. The patterns in these diagrams hinted at an underlying symmetry
 102 governing the strong nuclear force, and ultimately led to the invention of the very
 103 first quark model by Gell-Mann and Zweig in 1964 [21]. This model proposed that
 104 all of the hadrons were actually composed of even smaller particles, which Gell-Mann
 105 dubbed “quarks”. The quark model was able to explain the patterns seen in Figure 1.2
 106 by introducing three different types of fermionic quarks—up, down and strange—along
 107 with their corresponding anti-quarks. Baryons would then be composed of three such

²The “strangeness” being referred to in this section was introduced a few years before the very first quark model, but it now has the modern interpretation which is directly related to the number of strange and anti-strange quarks within a hadron.

³Namely $SU(3)$, but this is a history lesson. Also the path from $SU(3)$ to patterns of this type is long and arduous, involving a thorough understanding of representation theory.

⁴The original paper on the Eightfold Way does not contain any of these diagrams, but there are discussions about the properties of particles that should exist if the theory were correct, but had not been observed [15].

108 quarks, whereas mesons would be composed of quark and anti-quark pairs. If the
109 quark model were correct, the number of fundamental building blocks of matter would
110 again decrease from over 100 to just 14: electrons, muons, electron neutrinos, muon
111 neutrinos, up quarks, down quarks, strange quarks, and all of their corresponding
112 anti-particles.

113 Initially, many physicists believed that the quarks from this model were just a
114 mathematical abstraction [22]. This possibility did not stop Sheldon Glashow and
115 James Bjorken from extending the quark model less than a year after its inception by
116 introducing a fourth quark: the charm [23]. This new quark was primarily introduced
117 to equalize the number of leptons (four at the time: electron, muon, and their re-
118 spective neutrinos) with the number of quarks. The theory was mostly aesthetic [24]
119 in that the charm quark was not explicitly required by any known mechanisms. It
120 was only after the Glashow-Iliopoulos-Maiani (GIM) mechanism was introduced in
121 1970 [25] that the existence of the charm quark became necessary. This mechanism
122 helped explain why neutral kaons decayed into two muons at a much lower rate than
123 expected, but it required the existence of a quark with the same charge as the up
124 quark but with a much larger mass.

125 The notion that protons and neutrons were fundamental particles was also being
126 challenged on the experimental side. The deep inelastic scattering experiments at the
127 Stanford Linear Accelerator Center (SLAC) performed by Kendall, Friedman, and
128 Taylor in 1968 [26]–[28] revealed unexpected⁵ behavior when probing the structure
129 of the proton: it appeared to be composed of point-like particles. These experiments
130 were performed by firing electrons at stationary protons and measuring the energy
131 distributions of the scattered electrons at different scattering angles. An example
132 of such a distribution for electrons with initial energies of 10 GeV scattered at 6
133 degrees can be seen in Figure 1.3. The large spike on the left side of the distribution
134 corresponds to the elastic scattering of the electron off the proton, which was well
135 understood at the time [29]. The “bumps” observed at lower values of the scattered
136 electron energy were also well understood [30], and they correspond to the “shallow”
137 inelastic scattering of the electron off the proton, where the proton gets excited into a
138 so-called *resonance* state (like the Δ baryon). However, the “background” underneath
139 the bumps and the apparent continuum of events at even lower values of the scattered

⁵Depending on who you asked at the time, both the three and four quark models were not universally accepted.

140 electron energy corresponded to a host of unknown particles being produced. This
 141 host of particles appeared to grow with increasing scattering angle and decreasing
 142 scattered electron energy, which ultimately led to the conclusion that the proton was
 143 composed of point-like particles that were being “knocked out” of the proton by the
 144 incoming electron [26], [31].

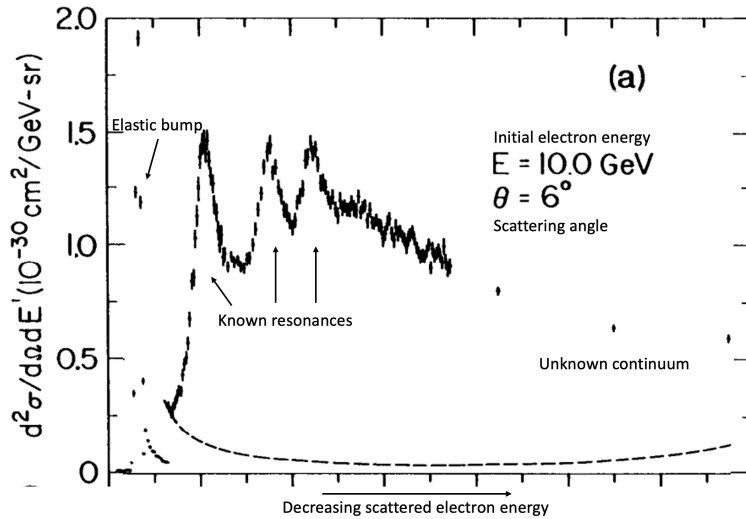


Figure 1.3: The energy distribution of electrons scattered off of protons at an initial electron energy of 10 GeV and a scattering angle of 6 degrees. The large spike on the left side of the distribution corresponds to the elastic scattering of the electron off the proton, and the “bumps” correspond to the inelastic scattering of the electron off the proton. The “background” underneath the bumps and the apparent continuum of events at even lower values of the scattered electron energy correspond to a mess of unknown particles being produced. The behavior of this continuum with respect to the scattering angle and the scattered electron energy ultimately led to the conclusion that the proton was not fundamental.

145 While many physicists were perfectly happy to interpret these point-like parti-
 146 cles as the very same quarks from the aforementioned quark model(s), they received
 147 the much more noncommittal name **partons** after Richard Feynman’s parton model
 148 of hadrons [32]. The association of these partons with quarks was not universally
 149 accepted⁶ until the discovery of the J/ψ meson in 1974 [33]. In the meantime, the
 150 theoretical description of the strong nuclear force was closing in on its final form.

⁶No acceptance of any model is a step function, but the discovery of J/ψ seems to be a turning point in literature.

151 The formulation of Quantum ChromoDynamics (QCD) in the early 1970s by Gell-
152 Mann, Fritzsch, and Leutwyler [34] resolved many of the issues that were present in
153 the initial quark models⁷. QCD introduced the concept of color charge, which all of
154 the quarks would carry. The mediating bosons of the strong interaction—known as
155 **gluons**—were also introduced, carrying color charge as well.

156 While QCD gave a solid mathematical description of the strong interaction, it
157 wasn’t until the discovery of **asymptotic freedom** [35], [36] by Gross, Wilczek, and
158 Politzer in 1973 that the theory became experimentally testable. Asymptotic freedom
159 refers to the property that the strong interaction becomes weaker at higher energies,
160 allowing for QCD calculations to be performed using perturbative techniques. This
161 discovery allowed theorists to use QCD to make predictions of the results of very
162 high energy particle collision experiments. The first QCD prediction to be experimen-
163 tally verified came from the Positron-Electron Tandem Ring Accelerator (PETRA)
164 in 1979 [37], which experimentally confirmed the existence of gluons [38]. With ex-
165 perimental verification of QCD, it became clear that the association of partons with
166 quarks was indeed incorrect: they are both quarks *and* gluons.

167 In addition to the theory of QCD, the theory of electroweak interactions was
168 also being developed during the 1960s by Glashow, Weinberg, and Salam [39], [40].
169 With this new theory came the prediction of four⁸ new bosons: the Higgs boson, the
170 charged W^\pm bosons, and the neutral Z^0 boson. With the combined theories of the
171 electroweak and strong interaction, the **Standard Model** of particle physics—which
172 describes the now 61⁹ fundamental particles and how they interact—was complete.

173 1.2 The Standard Model

174 The Standard Model of particle physics is a **quantum field theory** (QFT) that
175 describes the interactions between all¹⁰ of the fundamental particles. QFTs describe
176 the dynamics of a quantum system in terms of fields, which are functions of space and

⁷For example, the wavefunction of the Δ^{++} baryon under the first quark model was not anti-symmetric, which is a requirement for fermions.

⁸The Higgs mechanism (which predicts the existence of the Higgs boson) came before electroweak unification [41], but it was a requirement for the theory.

⁹There are many ways to count fundamental particles, but this particular number is obtained by: 6 leptons ($\times 2$ for anti-leptons), 6 quarks ($\times 3$ for each color, $\times 2$ for anti-quarks), 1 gluon ($\times 8$ for color), 1 photon, the W and Z bosons, and the Higgs boson.

¹⁰Ignoring potential gravitons [42] or dark matter candidates [43]

177 time. The fields are the fundamental objects of QFT, and their excitations correspond
178 to the particles that are observed in nature. The Standard Model fields can be broken
179 down into three sectors, which will be discussed in the following sections.

180 **1.2.1 The gauge sector**

181 The gauge sector of the Standard Model corresponds to the spin-one bosons that
182 mediate the strong and electroweak interactions. In a general sense, this sector corre-
183 sponds to the mediating particles for three of the four fundamental forces: the strong
184 nuclear force, the weak nuclear force, and the electromagnetic force. The fourth
185 fundamental force—gravity—is not included in the Standard Model, as it is not yet
186 understood from a quantum perspective [44].

187 The symmetry group of the gauge sector is given by

$$\text{SU}(3)_c \times [\text{SU}(2)_L \times \text{U}(1)_Y]. \quad (1.1)$$

188 $\text{SU}(3)_c$ is the symmetry group of the strong interaction, which is described by the QFT
189 known as Quantum ChromoDynamics (QCD). The subscript c stands for “color”,
190 indicating that the gauge fields in QCD (gluons) only couple to colored objects. QCD
191 will be discussed in more detail in Section 1.3. The symmetry group of the electroweak
192 interaction is $\text{SU}(2)_L \times \text{U}(1)_Y$, where the subscript L stands for “left-handed” and the
193 subscript Y stands for “weak hypercharge”. Again, these subscripts indicate the types
194 of objects to which the corresponding gauge fields couple. For example, the gauge
195 fields of $\text{SU}(2)_L$ only couple to left-handed objects, and the gauge fields of $\text{U}(1)_Y$
196 only couple to weakly hypercharged objects. Initially, there are four massless gauge
197 fields in the electroweak theory ¹¹. After the spontaneous symmetry breaking of the
198 Higgs mechanism [41], these fields mix to give rise to three massive gauge fields and
199 one massless gauge field. The three massive gauge fields correspond to the familiar
200 W^\pm and Z^0 bosons, which are the mediating bosons of the weak interaction. The
201 massless gauge field corresponds to the photon, which mediates the electromagnetic
202 interaction.

¹¹Three corresponding to the generators of $\text{SU}(2)$, one corresponding to the generator of $\text{U}(1)$.

203 **1.2.2 The scalar sector**

204 The scalar sector of the Standard Model is quite lonely, and only corresponds to
205 one spin-zero field: the Higgs [41]. As mentioned in the previous section, the Higgs
206 mechanism that corresponds to this field is responsible for the acquisition of mass
207 by the W^\pm and Z^0 bosons. The Higgs field also couples to all of the fermions in the
208 Standard Model, but the mass acquisition procedure is *slightly* different¹² from the
209 massive bosons. The associated Higgs boson was discovered by the A Toroidal LHC
210 Apparatus (ATLAS) and Compact Muon Solenoid (CMS) collaborations in 2012 [45],
211 [46], and was the last major piece of the Standard Model to be experimentally verified.

212 **1.2.3 The fermionic sector**

213 The fermionic sector contains all of the spin one-half particles (quarks and leptons) in
214 the Standard Model. It is often convenient to group these particles into three genera-
215 tions, where each generation is identical except for the masses of the particles. It is
216 even *more* convenient to group the fermions within each family into multiplets, where
217 the members of the multiplet are related to each other by transformations within the
218 gauge group of the Standard Model (Equation 1.1). In other words, the fermions
219 within a particular multiplet can only be transformed to fermions within the same
220 multiplet. A table of the fermions in the Standard Model and their corresponding
221 multiplets can be seen in Table 1.1. The indices L and R correspond to the chirality
222 of the fields, and the indices r , g , and b represent the color charge of the fields. The
223 color charges are only non-zero for the quarks, making them the only fermions that
224 couple to the gauge fields of the strong interaction (gluons).

225 **1.3 Quantum chromodynamics**

226 While the discussions above have been *mostly* general, the novel research presented
227 in this thesis is centered around the strong nuclear force. As such, this section will
228 delve into the details of this mysterious force and its interesting properties.

¹²It's still spontaneous symmetry breaking, but within the Yukawa part of the electroweak La-
grangian.

Table 1.1: The fermions of the Standard Model for each generation and their corresponding multiplets. The Standard Model does not allow for fermions to leave their respective multiplets.

Gen.	Left-handed quarks	Right-handed up quarks	Right-handed down quarks	Left- handed leptons	Right- handed leptons
1 st gen.	$\begin{pmatrix} u_L^r & u_L^g & u_L^b \\ d_L^r & d_L^g & d_L^b \end{pmatrix}$	$(u_R^r \ u_R^g \ u_R^b)$	$(d_R^r \ d_R^g \ d_R^b)$	$\begin{pmatrix} \nu_{eL} \\ e_L \end{pmatrix}$	(e_R)
2 nd gen.	$\begin{pmatrix} c_L^r & c_L^g & c_L^b \\ s_L^r & s_L^g & s_L^b \end{pmatrix}$	$(c_R^r \ c_R^g \ c_R^b)$	$(s_R^r \ s_R^g \ s_R^b)$	$\begin{pmatrix} \nu_{\mu L} \\ \mu_L \end{pmatrix}$	(μ_R)
3 rd gen.	$\begin{pmatrix} t_L^r & t_L^g & t_L^b \\ b_L^r & b_L^g & b_L^b \end{pmatrix}$	$(t_R^r \ t_R^g \ t_R^b)$	$(b_R^r \ b_R^g \ b_R^b)$	$\begin{pmatrix} \nu_{\tau L} \\ \tau_L \end{pmatrix}$	(τ_R)

229 1.3.1 The QCD Lagrangian

The dynamics of the Standard Model fields and how they interact are completely encoded within the Lagrangian of the theory, which can be used to calculate experimental observables like cross-sections and decay rates. However, the Lagrangian of the Standard Model is fairly long [47], and often not particularly insightful when trying to study a specific aspect of the theory. As such, when studying QCD, it is often useful to throw away the electroweak gauge fields, leptons, and scalars to look at only the QCD Lagrangian [48],

$$\mathcal{L}_{QCD} = -\frac{1}{4}F_{\mu\nu}^A F^{A\mu\nu} + i\bar{q}\gamma^\mu \left(\partial_\mu + ig_s \frac{1}{2}\lambda^A \mathcal{A}_\mu^A \right) q - \bar{q}_R \mathcal{M} q_L - \bar{q}_L \mathcal{M}^\dagger q_R - \theta\omega,$$

230 where all repeated indices are summed over.

231 The gluons are described by the vector gauge field \mathcal{A}_μ^A , with index A representing
232 one of the eight color labels. These eight components belong to the color group
233 $SU_c(3)$, which is the gauge group of QCD. The corresponding coupling constant is
234 g_s , and the field strength tensor $F_{\mu\nu}^A$ is given by

$$F_{\mu\nu}^A = \partial_\mu \mathcal{A}_\nu^A - \partial_\nu \mathcal{A}_\mu^A + g_s f^{ABC} \mathcal{A}_\mu^B \mathcal{A}_\nu^C, \quad (1.2)$$

235 where f^{ABC} are the structure constants [49] of $SU_c(3)$. Note that while this field
236 strength tensor shares the same letters as the electromagnetic field strength tensor
237 $F_{\mu\nu}$, the additional term $g_s f^{ABC} \mathcal{A}_\mu^B \mathcal{A}_\nu^C$ in Equation 1.2 separates QCD and QED in a
238 very fundamental way: the gluons are allowed to self-interact. This self-interaction is

239 a direct result of the non-vanishing structure constants of $SU_c(3)$ ¹³, and is responsible
240 for the challenging nature of QCD calculations.

241 The quarks are represented by the field q , where the color, flavor and spin indices
242 have been suppressed. In reality, the quark field q has:

243 • six flavor indices $\{u, d, s, c, b, t\}$,

244 • four spin indices $\{0, 1, 2, 3\}$, and

245 • three color indices $\{r, g, b\}$,

246 where all of these indices are being implicitly summed over in \mathcal{L}_{QCD} . Luckily, all of
247 the matrices $(\mathcal{A}_\mu^A, \lambda^A, \mathcal{M}, \gamma^\mu)$ act on separate sets of indices¹⁴. For example, the γ^μ s
248 only operate on the spin indices, whereas both the gluon fields \mathcal{A}_μ^A and Gell-Mann
249 matrices [15] λ^A operate on the color indices. These Gell-Mann matrices are the
250 generators of $SU_c(3)$ and satisfy the commutation relation

$$[\lambda^A, \lambda^B] = 2if^{ABC}\lambda^C. \quad (1.3)$$

251 The chiral quark fields q_L and q_R are defined as $\frac{1}{2}(1 - \gamma_5)q$ and $\frac{1}{2}(1 + \gamma_5)q$, respectively.
252 The mass matrix \mathcal{M} operates on the flavor indices, and its form depends on the choice
253 of basis for the quark fields [48]. It is often convenient to choose a basis where the
254 mass matrix is diagonal, which can be done by independent rotations of q_L and q_R in
255 $SU(6)$. Doing so gives the more familiar term

$$-\bar{q}_R \mathcal{M} q_L - \bar{q}_L \mathcal{M}^\dagger q_R = - \sum_{f=1}^6 \bar{q}_f m_f q_f, \quad (1.4)$$

256 where m_f is the mass of the quark with flavor f , and q_f is the flavor component of
257 the quark field. Note that this term completely violates the $SU(2) \times U(1)$ electroweak
258 symmetry, indicating that the given \mathcal{L}_{QCD} is determined *after* the spontaneous sym-
259 metry breaking described in the previous section.

260 These quark masses are also subject to **renormalization** [50], which is a process
261 that removes the infinities that arise from the self-interaction of the quarks and gluons.
262 The renormalization process results in the running of the quark masses with respect

¹³Structure constants of Abelian gauge groups like $U(1)$ are trivially zero.

¹⁴Really the components of the field corresponding to those indices.

263 to the energy scale μ of the interaction¹⁵. More simply, the quark masses are inversely
264 dependent on this energy scale: at large μ , the quark masses are small, and at lower
265 μ , the quark masses are large. At the energy scale $\mu \approx 2$ GeV (close to the mass of
266 the proton), the masses of the up, down, and strange quarks are approximately 2.2
267 MeV, 4.7 MeV, and 96 MeV, respectively [52].

268 The final term, known as the θ -term [53], is something of a mystery. It is a
269 scalar term that violates CP symmetry [54], and is often set to zero as there is no
270 experimental evidence for its existence. However, it is not clear why this term is zero,
271 as there is no symmetry that explicitly forbids it. This is known as the **strong CP**
272 **problem**, and is one of the biggest open questions in particle physics [55].

273 1.3.1.1 Brief aside: Why eight gluons?

274 The gluon field \mathcal{A}^A transforms under the adjoint representation of SU(3), which
275 is a representation of SU(3) on the vector space of its Lie algebra $\mathfrak{su}(3)$. As $\mathfrak{su}(3)$
276 has eight basis elements (for instance, the Gell-Mann matrices λ^A from above), the
277 adjoint representation of SU(3) is eight-dimensional. Thus the gluon field has eight
278 independent components, or, equivalently, there are eight gluons. In principle, QCD
279 could have been built on top of a U(3) gauge group, which would give rise to nine
280 gluons (as the dimension of U(n) is n^2). However, the singlet state in U(3) would be
281 required to be non-interacting; if it were, color neutral baryons would interact with
282 each other via the strong interaction at a much longer range [56]. Such interactions
283 have not been observed [57]. As there is no physical difference between U(3) with a
284 non-interacting singlet and SU(3), the simpler gauge group was chosen.

285 1.3.2 Properties of QCD

286 1.3.2.1 Confinement

287 One of the unique properties of QCD is the phenomenon of **confinement**, which is
288 the observation that quarks and gluons are never seen in isolation. Instead, they are
289 *confined* inside of the color neutral bound states known as hadrons. This property
290 is mostly understood in terms of the coupling constant g_s . The renormalization [58]

¹⁵They also depend on the *choice* of renormalization scheme, with the most commonly implemented one being minimal subtraction or MS [51].

of QCD gives rise to a g_s that varies with energy scale or distance. As the distance between two quarks increases, so too does g_s . At some point, the coupling becomes so strong that the energy required to separate the quarks is enough to create a quark-antiquark pair from the vacuum. Thus any attempts to separate a quark from a hadron will always result in the creation of a new hadron, making it impossible to observe single quarks in isolation.

The large coupling constant in this low energy regime makes it impossible to describe this phenomenon using perturbative techniques, so the exact mechanism of confinement is still not fully understood. However, it is often described using the phenomenological Lund string model [59]. In this model, the field lines of two quarks are pulled together due to the self-interaction of the gluons. This creates a string-like structure between the two quarks, with a potential given by

$$V(r) \approx -\frac{4}{3} \frac{\alpha_s}{r} + \kappa r, \quad (1.5)$$

where r is the distance between the two quarks, $\alpha_s = \frac{g_s^2}{4\pi}$ and κ is the string tension. This can be contrasted with the potential between two electrically charged particles, where the field lines are not pulled together and become less dense as the distance between the two particles increases. As such, the potential decreases with increasing distance, opposite to that of the Lund model. A schematic of these differences can be seen in Figure 1.4.

1.3.2.2 Asymptotic freedom

Just as the coupling constant becomes large at low energies and large distances, it also becomes small at high energies and small distances. This property is known as **asymptotic freedom**: at high enough energies, the quarks and gluons can be thought of as “free”, and their interactions can be modeled using perturbative QCD (pQCD). As discussed in Section 1.1, the discovery of asymptotic freedom in QCD was what allowed for the accurate predictions of the results of high energy particle collision experiments like SLAC [60] and PETRA [37]. The results of such experiments have also been used to calculate the value of the coupling constant itself at different energy scales, as shown in Figure 1.5. The value of α_s at the Z^0 mass is also given in the figure, which is the most accurate measurement of α_s to date [52].

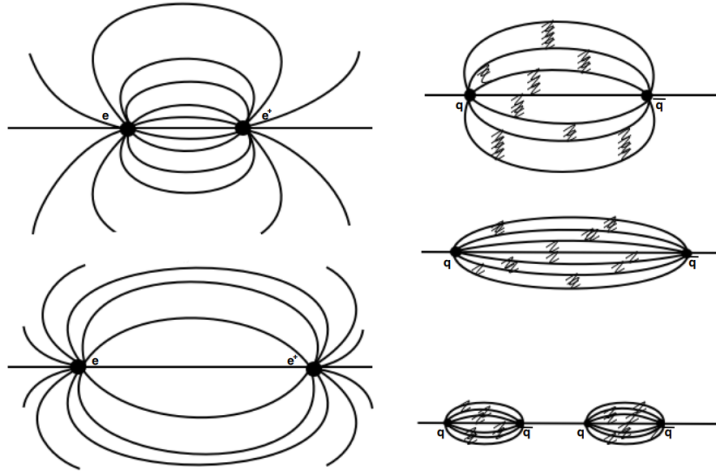


Figure 1.4: A schematic of the field lines between two electrically charged particles (left) and two quarks (right). The field lines between the quarks are pulled together due to the self-interaction of the gluons, whereas the electric field lines are not.

320 1.3.2.3 Jets

321 During high energy particle collisions (between two protons, for example), the con-
 322 stituent partons of the protons will sometimes scatter off each other in a way that con-
 323 verts most of their initial longitudinal momentum (along the collision axis) into trans-
 324 verse momentum (in the plane perpendicular to the collision axis). Such a scattering
 325 is often referred to as a **hard scattering**. Because the momentum transfer is large,
 326 the cross-section of the parton-parton scattering is calculable using pQCD. Further-
 327 more, branching processes of the high momentum partons—like gluon radiation—can
 328 also be calculated perturbatively. Eventually, however, the partons will lose enough
 329 energy such that their behavior can no longer be described using perturbative tech-
 330 niques.

331 Luckily, the aforementioned Lund model is well-equipped to deal with lower energy
 332 partons. Under the Lund model, as these colored partons move away from each
 333 other, the force between them increases until there is enough energy to produce a
 334 quark-antiquark pair (as discussed in Section 1.3.2.1). This process—known as string
 335 fragmentation—continues until the partons are no longer energetic enough to move
 336 away from each other, at which point they hadronize into a large number of color
 337 neutral bound states. These particles are roughly collimated in the direction(s) of

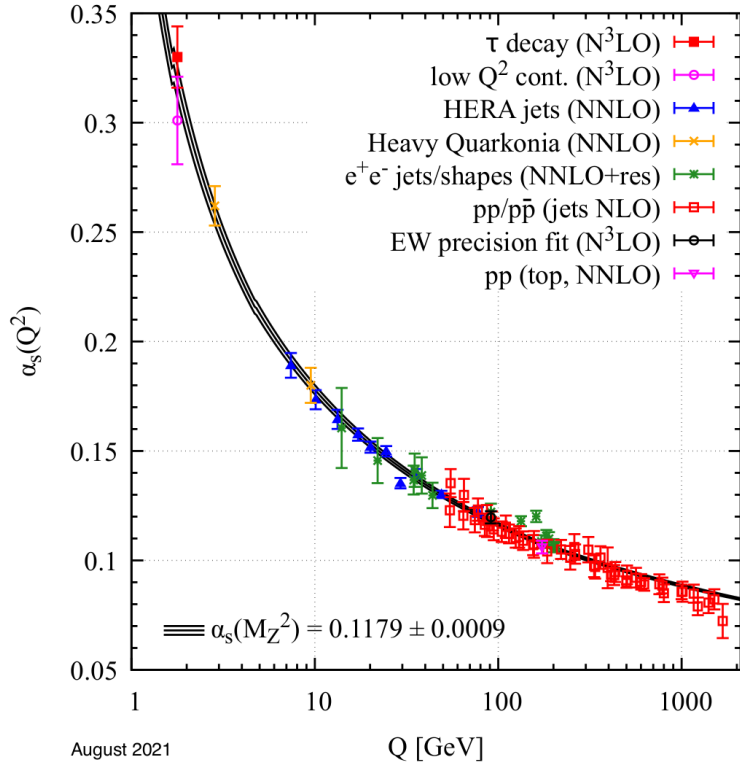


Figure 1.5: The value of the strong coupling constant α_s as a function of momentum transfer Q , which represents the energy scale of the interaction.

338 the initial hard scattering, forming sprays of hadrons known as **jets**. A diagram
 339 depicting the formation of a jet from an initial hard scattering of partons can be seen
 340 in Figure 1.6.

341 1.3.2.4 Flavor conservation

342 One interesting feature of the interactions in QCD is that all **flavor** quantum numbers
 343 are conserved. Specifically, the number of quarks minus the number of anti-quarks of
 344 each flavor is a conserved quantity in every strong interaction¹⁶. In this thesis, the
 345 most important flavor quantum number is **strangeness**, which is defined as

$$S = -(n_s - n_{\bar{s}}), \quad (1.6)$$

¹⁶Conservation of the “historical” flavor quantum number *isospin* (from Section 1.1), which is $+\frac{1}{2}$ for up quarks and $-\frac{1}{2}$ for down quarks, is equivalent to the conservation of $n_{u,d} - n_{\bar{u},\bar{d}}$ when baryon number is considered. Baryon number is an absolutely conserved quantum number in the Standard Model [52], and (anti-)quarks have baryon number $(-)\frac{1}{3}$.

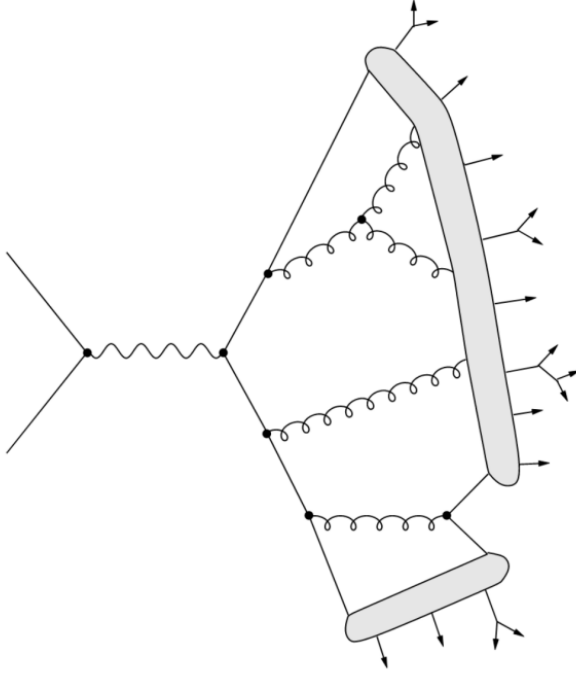


Figure 1.6: A diagram depicting the formation of a jet within the Lund model from an initial hard scattering of partons, adapted from [61]. The vertices represent perturbative QCD processes, the shaded regions represent string fragmentation/hadronization, and the outgoing arrows represent the resulting hadrons (which may decay further).

346 where n_s is the number of strange quarks and $n_{\bar{s}}$ is the number of strange anti-quarks.
 347 The “minus” sign in front of the expression indicates that the strangeness of a strange
 348 quark is negative (-1), and the strangeness of a strange anti-quark is positive ($+1$).
 349 This convention is chosen¹⁷ to make the signs of these “flavor charges” consistent
 350 with the signs of the electric charges of these quarks, which are $-\frac{1}{3}$ for the strange
 351 quark and $+\frac{1}{3}$ for the strange anti-quark. Strangeness conservation has an interesting
 352 consequence for particle collisions between atomic nuclei: as the total strangeness of
 353 these nuclei (protons and neutrons) is zero, the number of strange and anti-strange
 354 quarks produced from the strong interaction during these collisions must be equal.
 355 In other words, the production of strange quarks in these collisions must come in the
 356 form of strange quark-anti-quark ($s\bar{s}$) pairs.

¹⁷Really this is a historical convention that stems from the fact that “strangeness” was introduced as a concept before the existence of any quark models, as mentioned in Section 1.1.

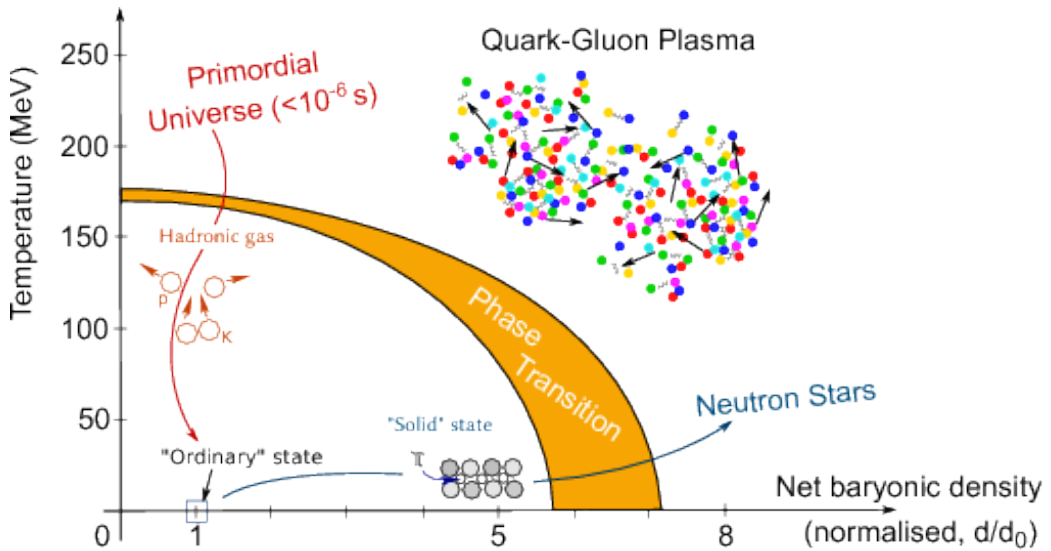


Figure 1.7: A phase diagram of the QGP, taken from [64]. The axes are temperature and baryon density, and the orange band represents the phase transition from normal hadronic matter to the QGP.

357 1.4 The Quark-Gluon Plasma

358 One of the consequences of the asymptotic freedom of QCD is the prediction of
 359 a new state of matter at extreme temperatures and densities: the **quark-gluon**
 360 **plasma** (QGP) [62], [63]. In this plasma, the quarks and gluons are not confined
 361 inside hadrons, and instead behave as quasi-free particles. This is analogous to an
 362 electromagnetic plasma, where electrons and protons are dissociated from their atoms.
 363 A phase diagram of this plasma can be seen in Figure 1.7. This diagram has two
 364 axes: temperature and baryon density. Increasing *either* of these quantities beyond
 365 a certain threshold will cause a phase transition from normal hadronic matter to the
 366 QGP. Similarities can be drawn between this phase diagram and that of a snowball:
 367 heating *or* squeezing a snowball will cause it to melt into a liquid¹⁸.

368 Numerical simulations of QCD on a lattice **LatticeQCD** (known as lattice QCD
 369 or lQCD) have shown that the phase transition from ordinary hadronic matter to the
 370 QGP requires a temperature of around 160 MeV whenever the net baryon density is
 371 zero **LatticeQCD.CriticalTemp**, as highlighted on the left side of Figure 1.7.

¹⁸Be careful: if you continue to heat up the snowball enough, or squeeze hard enough, it will undergo another phase transition into the QGP.

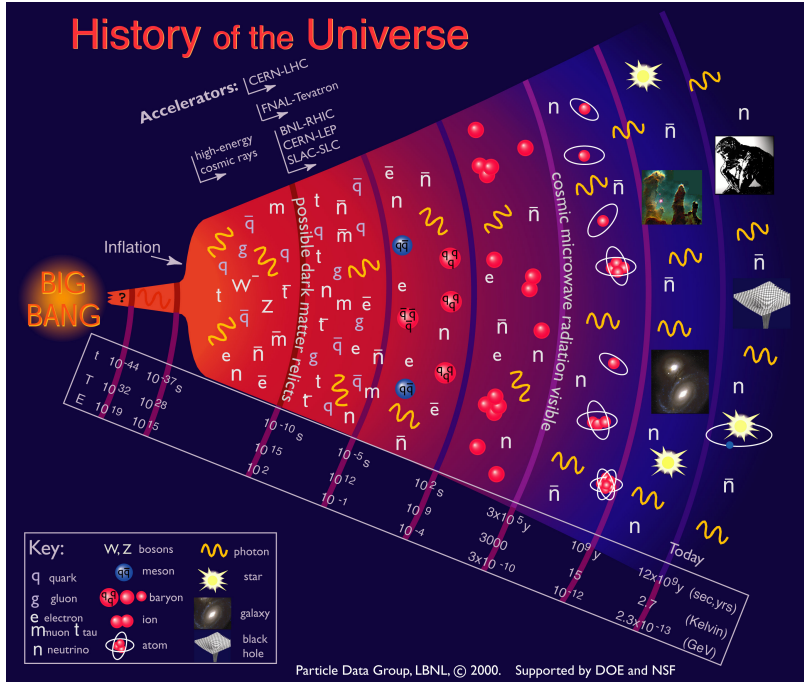


Figure 1.8: A schematic of the evolution of the universe, taken from [52]. The QGP phase of the universe on this diagram lies roughly between 10^{-10} and 10^{-5} seconds after the Big Bang.

372 Studying the QGP and its formation is interesting for a number of reasons, but
 373 those reasons often get lost in the cosmological hype: the universe is thought to have
 374 been composed of this plasma in the first few microseconds after the Big Bang [65].
 375 Thus studying the QGP *can* give insight to the early universe and its expansion,
 376 which is schematically represented in Figure 1.8. It is also postulated that QGP
 377 formation occurs in the cores of neutron stars [66], giving another avenue of interest
 378 for astrophysicists.

379 However, the QGP is also very interesting from a purely particle physics per-
 380 spective; it is a highly non-perturbative QCD system that can be generated in a
 381 laboratory setting. Studying this plasma and its properties can help illuminate the
 382 dark, confounding corners of QCD that are not yet understood—like confinement. Un-
 383 fortunately producing this plasma in a laboratory setting is not a trivial task, and
 384 requires¹⁹ colliding heavy ions at very high energies.

¹⁹There are hints of QGP formation in proton-proton collisions, which will be discussed in Section 1.6

385 **1.5 Using Heavy-Ion Collisions to Study the**
386 **QGP**

387 The QGP phase diagram in Figure 1.7 shows two methods for producing the QGP:
388 increasing the system's temperature or increasing its baryon density. Luckily these
389 two methods are not mutually exclusive:

- 390 • Baryon density can be increased by looking at systems with a lot of baryons
391 packed together (like the nucleus of a lead atom)
- 392 • Temperature can be increased by smashing the aforementioned systems together
393 at higher energies (like in a particle accelerator)

394 Thus one of the best (and only) ways to study the QGP in a laboratory setting is
395 through relativistic **heavy ion collisions**: the smashing together of two heavy nuclei
396 at very high energies using a particle accelerator.

397 Unfortunately, producing the QGP in this manner has a major drawback; while
398 it is possible to heat up the system beyond the critical temperature required for
399 QGP formation, the system expands and cools *very* quickly. For example, the QGP
400 produced by colliding lead ions with center-of-mass energy $\sqrt{s_{NN}} = 2.76 \text{ TeV}$ at the
401 Large Hadron Collider (LHC) only lasts for around $3 \text{ fm}/c$ [67], or 10^{-23} seconds . A
402 diagram depicting the formation and evolution of the QGP in a heavy ion collision
403 can be seen in Figure 1.9. This diagram can be split up into the following stages:

- 404 1. The Lorentz-contracted nuclei approach each other at very high energies, and
405 the partons within the nuclei scatter off each other ($t = 0 \text{ fm}/c$).
- 406 2. As new partons are created from the initial scatterings, the energy density of
407 the system increases. Eventually this energy density is high enough to create
408 the QGP ($t \approx 1 \text{ fm}/c$).
- 409 3. Once the QGP is formed, it expands and cools in a hydrodynamic manner.
- 410 4. After the QGP cools below the critical temperature, the partons begin to
411 hadronize, resulting in the formation of a hadron gas ($t \approx 3 \text{ fm}/c$).

412 5. The hadron gas will continue to expand until the hadrons within the gas are no
413 longer strongly interacting with each other ($t \approx 10 \text{ fm}/c$). This is often broken
414 up into two stages:

- 415 • The hadrons cease to interact *inelastically*, called **chemical freeze-out**.
416 • The hadrons cease to interact *elastically*, called **kinetic freeze-out**.

417 6. If a detector is built within a few meters around the collision point, the final
418 state hadrons can be observed ($t \approx 10^{15} \text{ fm}/c$).

419 The last stage of this diagram is perhaps the most frustrating: it is only possible
420 to study the QGP by observing the final state hadrons. Luckily, there are some
421 key observables associated with those final state hadrons that can shed light on the
422 formation and evolution of this exciting plasma. Before those observables can be
423 discussed, however, it is necessary to introduce a key concept in heavy ion collisions:
424 the centrality of the collision.

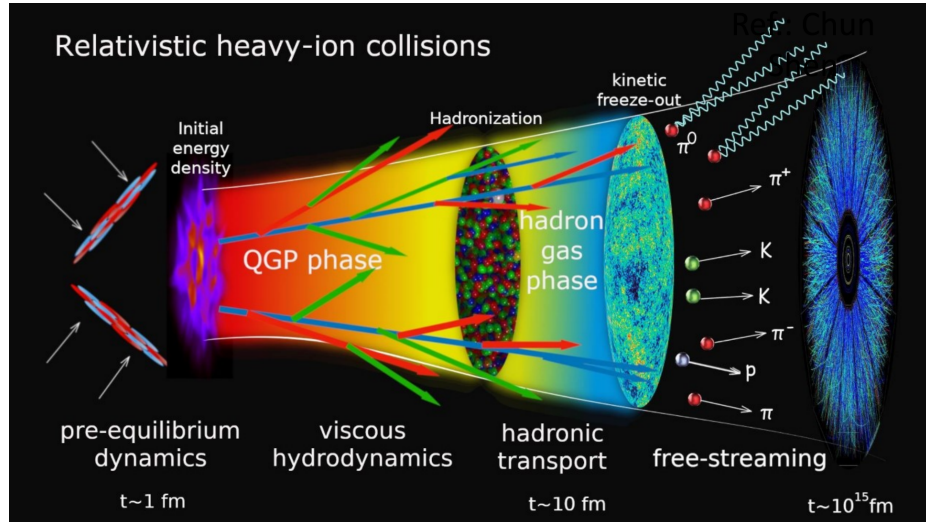


Figure 1.9: A schematic of the formation and evolution of the QGP in a heavy ion collision. The QGP is formed in the overlap region of the two colliding nuclei, and then expands and cools very quickly.

425 **1.5.1 Collision centrality**

426 The very first step of the heavy ion collision process involves the scattering of the
427 partons within the two nuclei. However, these nuclei are not point-like objects: they
428 have a finite size, and therefore need not collide “head-on”. Instead, the nuclei
429 can collide at different **impact parameters** (commonly denoted as b), as shown in
430 Figure 1.10. The impact parameter is defined as the distance between the centers
431 of the two nuclei, measured in the transverse plane (the plane perpendicular to the
432 initial directions of the nuclei). Collisions with a large impact parameter give rise to
433 *spectator* nucleons, which do not participate in the collision and continue traveling
434 as they please.

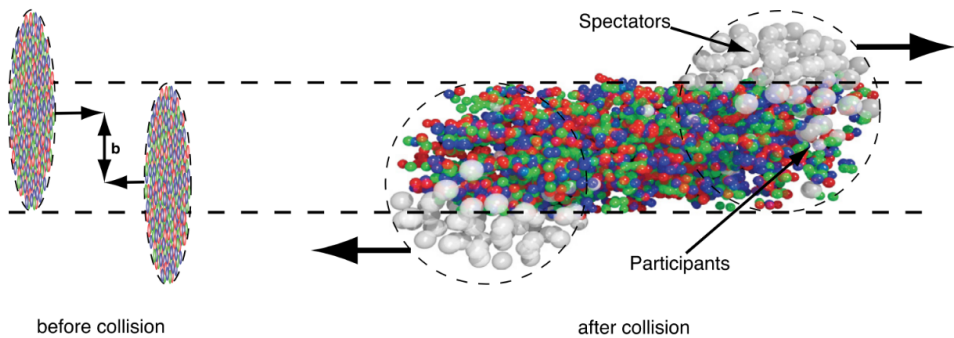


Figure 1.10: A schematic of a heavy ion collision with impact parameter b , taken from [68].

435 The impact parameter is very important when studying the QGP for a fairly
436 straightforward reason: as the impact parameter decreases, the number of partonic
437 scatterings increases, which in turn increases the energy density of the system. In
438 some sense, the size of the impact parameter determines whether or not the QGP is
439 formed in the subsequent stages of the collision. As such, characterizing heavy ion
440 collisions by their impact parameter is quite useful. Unfortunately, much like the
441 QGP, the impact parameter is not directly measurable and must be inferred from the
442 final state hadrons.

443 Instead of classifying collisions based off their unobtainable impact parameter,
444 they are instead classified by their **collision centrality**. The collision centrality is

445 defined as

$$c = \frac{\int_0^b d\sigma/db' db'}{\int_0^\infty d\sigma/db' db'} = \frac{1}{\sigma_{AA}} \int_0^b \frac{d\sigma}{db'} db', \quad (1.7)$$

446 where σ_{AA} is the total cross section of the nucleus-nucleus (A-A) collision. As this
447 number is strictly between 0 and 1, it is often expressed as a percentile: 0% corre-
448 sponds to the most central collisions (lowest impact parameters), and 100% corre-
449 sponds to the most peripheral collisions (highest impact parameters). If a monotonic
450 relationship between b and the number of final state particles seen in the detector is
451 assumed, the collision centrality can be experimentally determined [69]. The number
452 of final state particles from a collision is called the **multiplicity** of the collision, and
453 is often denoted as N_{ch} . The subscript ch indicates that only charged particles are
454 counted, as neutral particles are not seen by most detectors.

455 In practice, the collision centrality percentiles are usually determined by looking
456 at the distribution of events as a function of the signal (effectively N_{ch}) as measured
457 by a particular detector. The percentile for a specific event can then be determined
458 by integration:

$$c \approx \frac{1}{\sigma_{AA}} \int_{N_{ch}}^\infty \frac{d\sigma}{dN'_{ch}} dN'_{ch}, \quad (1.8)$$

459 where N_{ch} is the multiplicity of the event in question. An example of separating
460 events into centrality percentiles using this method can be seen in Figure 1.11. In
461 this plot, Pb-Pb collisions are characterized by their event activity in the ALICE
462 VZERO detector (which will be discussed in more detail in the next chapter). The
463 red points correspond to fits obtained using Monte Carlo simulations based off of the
464 Glauber model [69], [70]. The Glauber model [71] is a geometric model that treats
465 the nuclei as a collection of nucleons, and models the collisions as a superposition of
466 binary nucleon-nucleon collisions. This model gives a relationship between the impact
467 parameter b , the number of participating nucleons N_{part} , and the number of binary
468 nucleon-nucleon collisions N_{coll} . While not of particular import to this thesis, fitting
469 the Glauber model to the data actually allows for the determination of the impact
470 parameter corresponding to a given multiplicity percentile. The fact that the model
471 describes the data well also serves as a sanity check for the experimental estimation
472 of the collision centrality. In this thesis, the terms “multiplicity percentile” and
473 “collision centrality” will be used interchangeably.

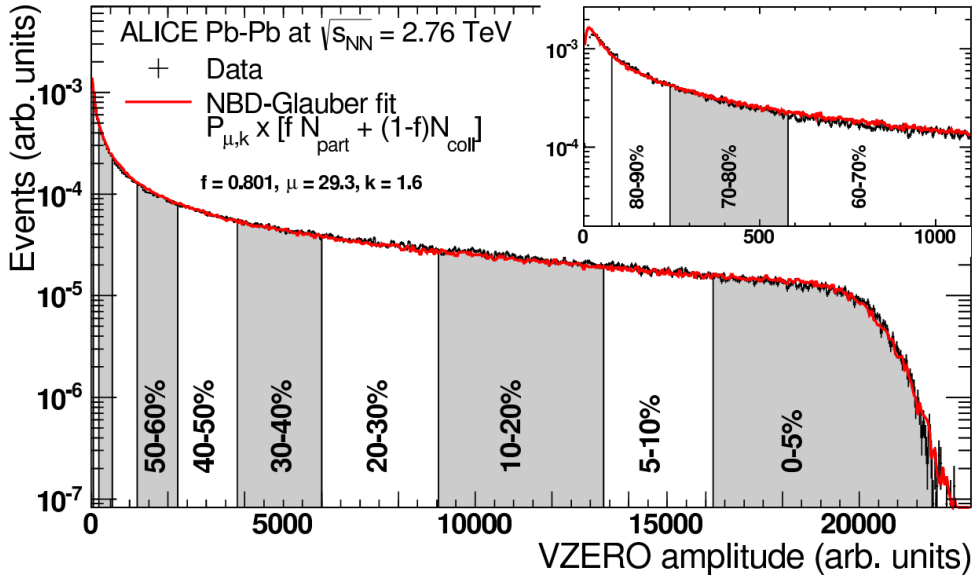


Figure 1.11: The distribution of Pb–Pb collision events as a function of event activity in the ALICE VZERO detector, taken from [70].

474 The approximation given by Equation 1.8 has an additional benefit: it allows for
 475 the determination of centrality without a clearly defined impact parameter. This is
 476 useful for proton-proton and proton-lead collisions, where the impact parameter is
 477 ill-defined.

478 1.6 Experimental signatures of QGP formation

479 As mentioned in Section 1.5, the QGP produced within a heavy ion collision is *very*
 480 short lived. As such, any attempt to study the QGP and its formation must be
 481 done using the detector-accessible final state hadrons. Luckily there are a number of
 482 signatures that can be used to study the QGP in experiment, including

- 483 • **jet quenching** [72], where the energy of a jet is heavily reduced due to its
 484 interactions with the QGP,
- 485 • **collective flow** [73], where the motion of the partons within the QGP is heavily
 486 influenced by the overall fluid-like medium, and

- 487 • **strangeness enhancement** [18], where the QGP exhibits an increase in the
488 production of strange quarks relative to up and down quarks.

489 These signatures are discussed in more detail in the following sections.

490 **1.6.1 Jet quenching**

491 The high momentum partons produced in the initial hard scatterings of heavy ion
492 collisions often traverse the QGP medium. Much like electron tomography, where the
493 passage of electrons through an atomic medium can give insight to the structure of the
494 atoms within, these high momentum partons can be used to probe the QGP. These
495 colored partons interact with the colored medium, losing energy in the process. As
496 discussed in Section 1.3.2.3, these partons are never observed individually; instead,
497 they hadronize into a spray of particles known as a jet. Thus the energy lost by
498 the parton is not observed directly, but rather as a reduction in the energy of the
499 resulting jet. This phenomenon is known as **jet quenching**, and is one of the most
500 well studied signatures of QGP formation.

501 Experimentally, this quenching is observed by studying *dijets*. While the term
502 “jet” refers to a single spray of particles observed in the detector, the initial hard
503 scattering responsible for the formation of the jet corresponds to the production of
504 *two* high momentum partons. Traveling in opposite directions in the transverse plane,
505 these partons often produce two jets that are back-to-back in φ (the azimuthal angle
506 in the transverse plane). These two jets are collectively referred to as a dijet. In pp
507 collisions, the energy of the two jets is roughly equal as the corresponding partons
508 don’t lose energy to a medium. In heavy ion collisions, however, the partons lose
509 energy to the QGP due to gluon radiation and elastic scattering with the medium’s
510 constituents [74]. If one of the two partons has a larger path length through the
511 QGP, it will lose more energy than the other parton, resulting in an imbalance in the
512 energy of the two jets. A schematic of this process for pp and A–A collisions can be
513 seen in Figure 1.12.

514 However, the path length within the QGP of the dijet-forming partons should be
515 roughly uniform, washing out this assymetry over a large event sample. As such, jet
516 quenching is experimentally observed by selecting high momentum “trigger” hadrons,
517 which most likely originated from the parton with the smaller QGP path length. The
518 jet corresponding to this higher momentum trigger—referred to as the “near-side” jet—

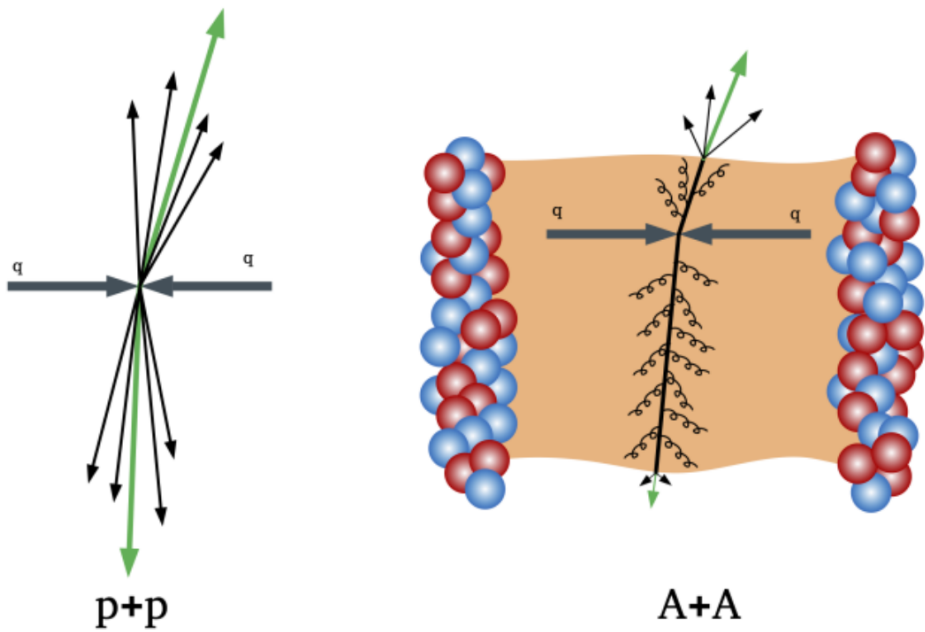


Figure 1.12: A schematic of the formation of dijets in $p+p$ and $A-A$ collisions, taken from [75].

is then compared with its partner jet, which would be 180° away in azimuth—called the “away-side” jet. The first collaboration to observe this jet quenching was the STAR collaboration at the Relativistic Heavy Ion Collider (RHIC) [76]. By looking at high transverse momentum hadrons produced in Au–Au collisions, they found that the away-side jet began to “disappear” as the centrality of the collision increased, as shown in Figure 1.13. This disappearance is due to the away-side jet losing energy to the QGP, such that the corresponding hadrons in the away-side fall below the momentum cutoff.

1.6.2 Collective flow

The QGP is a strongly interacting medium, whose constituent partons are heavily coupled to their surroundings. Just as the pebbles within a river get swept up in the flow of the water, the partons within the QGP are influenced by the flow of this medium. This flow manifests itself by the presence of collective effects in the final state hadrons, which are often quantified using **collective flow** components. These

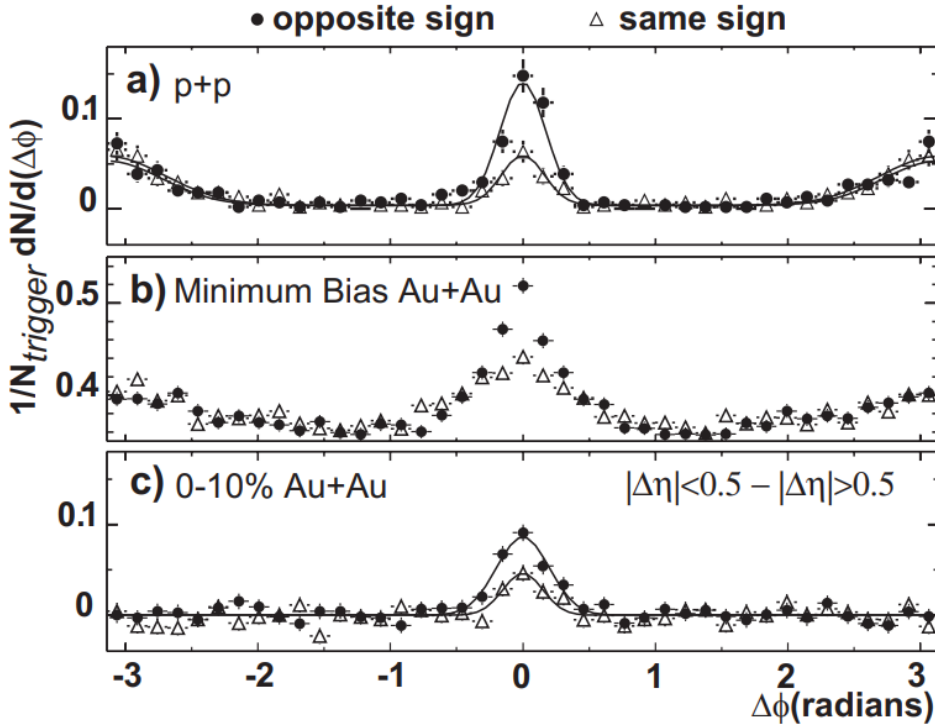


Figure 1.13: Hadron yields corresponding to the near-side jet (near $\Delta\varphi = 0$) and the away-side jet ($\Delta\varphi = \pm\pi$), taken from [76]. In pp and minimum bias Au–Au collisions, the away-side jet is present. However, at high centrality (0–10%), the away-side jet completely disappears.

533 flow components are obtained by expanding the final state hadron distribution in a
 534 Fourier series with respect to the azimuthal angle ϕ [77],

$$E \frac{d^3 N}{d^3 p} = \frac{1}{2\pi} \frac{d^2 N}{p_t dp_t dy} \left(1 + \sum_{n=1}^{\infty} 2v_n \cos[n(\phi - \Psi_R)] \right), \quad (1.9)$$

535 where E is the energy of the particle, p is its momentum, p_T is the momentum
 536 component in the plane transverse to the beam axis, y is the particle's rapidity, and
 537 Ψ_R is the reaction plane angle. This reaction plane angle is defined by the beam axis
 538 and the impact parameter vector. The Fourier coefficients

$$v_n = \langle \cos[n(\phi - \Psi_R)] \rangle \quad (1.10)$$

539 determine the “strength” of the corresponding flow component. The first two co-
 540 efficients, v_1 and v_2 , are referred to as **directed (radial) flow** and **elliptic flow**,

541 respectively. A non-zero directed flow originates from the space-momentum correla-
 542 tions in particle production from a longitudinally slanted source [78]. Directed flow
 543 is often much smaller than elliptic flow (by over an order of magnitude) [79], but it
 544 can still effect some of the measurements presented in this thesis (see Section ?? for
 545 more details).

546 Elliptic flow characterizes the anisotropy of the particle production in the trans-
 547 verse plane. This anisotropy is believed to be caused by the initial anisotropy of the
 548 collision geometry, where the overlap region of the colliding nuclei forms an “almond”
 549 shape. This almond is where the initial QGP is formed, which then hydrodynamically
 550 expands and thermalizes nearly instantaneously. The initial spacial anisotropy results
 551 in unequal QGP path lengths for the constituent partons, which ultimately results in
 552 an anisotropic momentum distribution for the corresponding hadrons (i.e. partons
 553 which travel through more medium lose more energy, as discussed in Section 1.6.1).
 554 A diagram depicting this process can be seen in Figure 1.14.

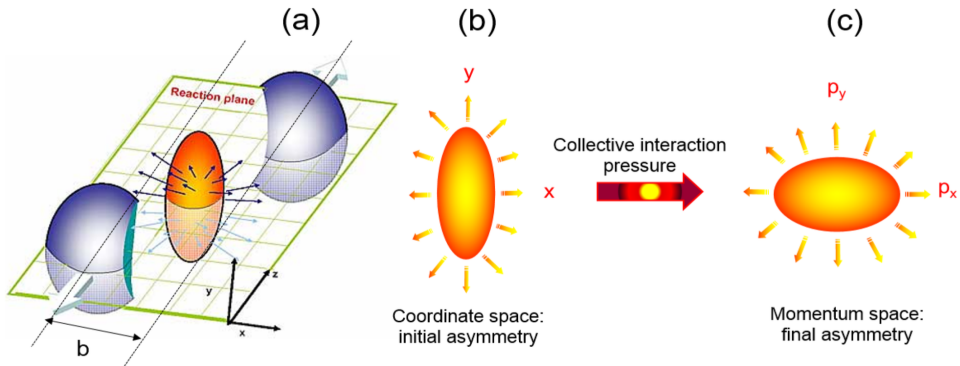


Figure 1.14: A schematic of the formation of elliptic flow in a heavy ion collision. The initial anisotropy in coordinate space results in a pressure gradient that causes a momentum space anisotropy in the final state hadrons.

555 1.6.2.1 Avoiding Ψ_R

556 Reconstructing the reaction plane angle Ψ_R is difficult as it must be done on an event-
 557 by-event basis [77]. As such, it is often more convenient to measure the collective
 558 flow components by looking at two-particle correlations in the azimuthal angle ϕ . In
 559 other words, the flow components can be obtained by looking at the distribution of

560 pairs of particles as a function of $\Delta\phi = \phi_1 - \phi_2$, where ϕ_1 and ϕ_2 are the azimuthal
561 angles of two (non-identical) particles. This distribution can be decomposed into a
562 Fourier series similar to Equation 1.9 [80],

$$\frac{dN^{\text{pair}}}{d\Delta\varphi} = a_0 + 2a_1 \cos \Delta\varphi + 2a_2 \cos 2\Delta\varphi + \dots, \quad (1.11)$$

563 where $v_n \equiv a_n/a_0$ are the very same flow coefficients from before. This bypasses the
564 need to reconstruct the reaction plane angle Ψ_R , but it also makes clear that any
565 analyses involving two-particle angular correlations (like the one presented in this
566 thesis) must be mindful of the presence of these coefficients (see Chapter ?? for more
567 details).

568 1.6.3 Strangeness enhancement

569 The earliest predicted signature of QGP formation was an increase in the production
570 of strange quarks relative to the production of up and down quarks [18]. Discovered
571 in 1981 by Johann Rafelski and Rolf Hagedorn, this *enhancement* in the produc-
572 tion of strange quarks in the QGP is referred to as **strangeness enhancement**.
573 As strangeness is conserved during strong interactions, the production of $s\bar{s}$ pairs
574 can only come from four Feynman diagrams (to lowest order in pQCD), shown in
575 Figure 1.15. The key insight by Rafelski and Hagedorn was that in the QGP, the
576 higher temperatures allow for the thermal production of $s\bar{s}$ pairs through gluon fusion
577 ($gg \rightarrow s\bar{s}$ or diagrams (a) (b) and (c) in Figure 1.15). This gluon fusion occurs much
578 faster than the quark-based production ($q\bar{q} \rightarrow s\bar{s}$ or diagram (d) in Figure 1.15),
579 and allows for the full chemical equilibration of strangeness in the QGP [81]. Such
580 an equilibration is not possible with only a hadronic gas phase [82] due to the much
581 slower interaction rates of hadrons.

582 Experimentally, strangeness production is measured by looking at the abundance
583 of strange hadrons relative to non-strange hadrons, like pions. For central heavy
584 ion collisions—both at the LHC and RHIC—these strange/non-strange particle ratios
585 are found to be consistent with a hadron gas in both thermal *and* chemical equilib-
586 rium [83], [84]. As mentioned previously, this is a strong indication that the QGP
587 is formed in these collisions. Furthermore, these particle ratios as measured in lower
588 multiplicity pp collisions at the LHC are found to be consistent with statistical mod-
589 els *without* chemical equilibration [85], [86]. Under the strangeness enhancement

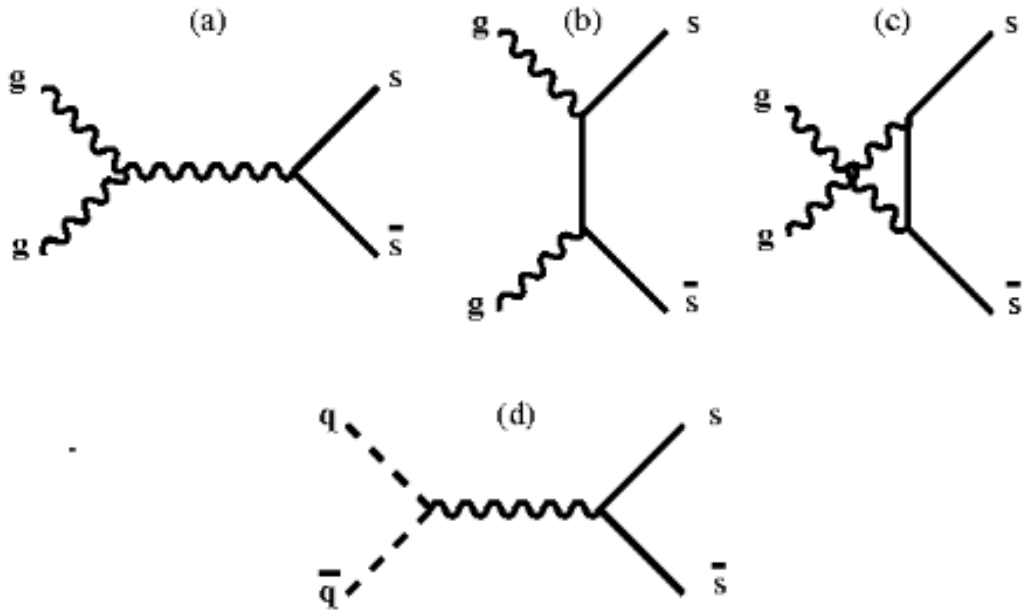


Figure 1.15: The four leading-order Feynman diagrams responsible for the production of $s\bar{s}$ pairs in the QGP, adapted from [18]. Diagrams (a), (b) and (c) are the gluon fusion processes, while diagram (d) is the quark-based process.

590 picture, this indicates that QGP formation does *not* occur in these lower multiplicity
 591 pp collisions.

592 However, filling in the gaps between low multiplicity pp collisions and high multi-
 593 plicity Pb–Pb collisions reveals a more complicated picture, as shown in Figure 1.16.
 594 The particle ratios seem to be consistent with a smooth transition between the two
 595 regimes, independent of collision system. In other words, the ratios in higher multi-
 596 plicity pp and p–Pb collisions match up nicely with the ratios in lower multiplicity
 597 Pb–Pb collisions. This indicates that the enhanced production of strange quarks is
 598 not exclusive to heavy ion collisions; there is an “onset” of strangeness enhancement
 599 occurring in lower multiplicity pp and p–Pb collisions. Furthermore, this enhancement
 600 is seen to scale with the number of strange quarks in the hadron: the Ω baryon (sss)
 601 exhibits the largest enhancement, while the proton (uud) sees virtually no increase.
 602 This provides even stronger evidence for the formation of a chemically equilibrated
 603 QGP, which no longer appears exclusive to heavy ion collisions.

604 While extensions to the aforementioned statistical models can describe these
 605 multiplicity-dependent particle ratios in a phenomenological manner [88], the mi-

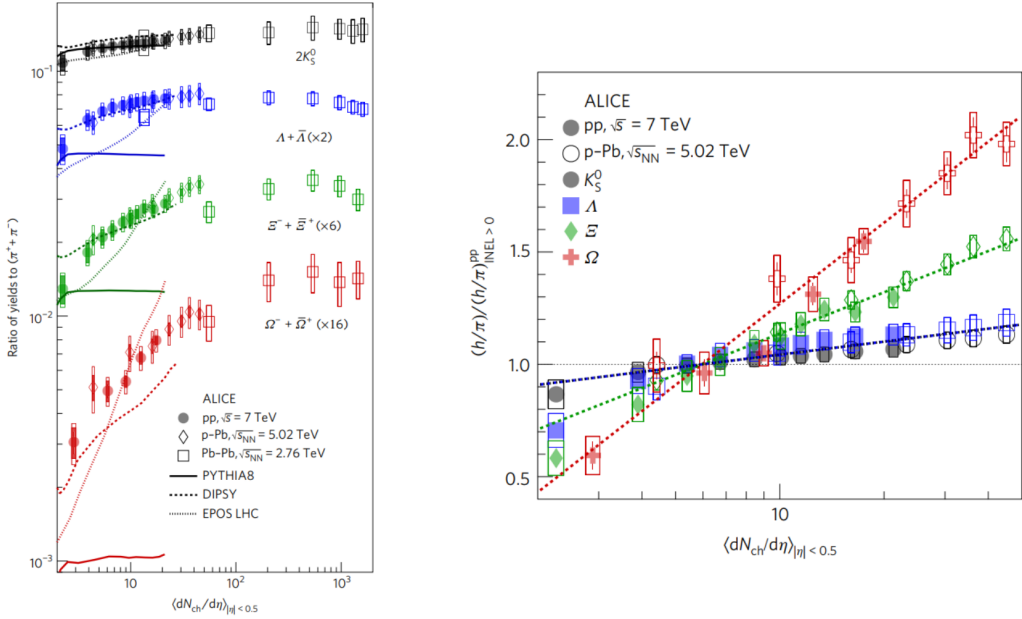


Figure 1.16: The particle ratios of strange hadrons to pions as a function multiplicity for different collision systems (left) and those same ratios normalized to an inclusive pp sample (right). The ratios appear to only depend on the multiplicity of the collision, and not the collision system. Taken from [87].

croscopic origins of this enhancement are not well understood. By investigating the production of strange hadrons in p–Pb collisions (where the onset is greatest), this thesis aims to shed light on the origins of this strange enhancement. However, it is necessary to first introduce some theoretical models to help interpret the results of this thesis.

1.7 Heavy-Ion Collision Models

Theoretical models of heavy ion collisions are pertinent to the understanding of QCD and the QGP. Without them, there would be no framework for interpreting the results from the very expensive experiments dedicated to studying this strongly interacting plasma. Unfortunately, due to the complexity of these heavy ion collision systems, there is no *single* model that can describe the entire collision evolution. Instead, the choice of model to compare a particular observable to depends very heavily on the observable in question. For example, some models treat the QGP phase of the

619 collision as a hydrodynamic system, washing out information about the initial par-
620 tonic scatterings [89]. This can be useful when trying to study bulk properties of
621 the QGP (like the v_2 from Section 1.6), but not-so-useful when studying jets and
622 their constituents. Other models focus more on the individual partonic scatterings
623 and subsequent hadronization, but do not include an explicit QGP phase [90], [91].
624 Such models are powerful tools for analyzing smaller collision systems (pp and lower
625 multiplicity p–Pb), but fail to capture many of the features observed in heavy ion
626 collision data. In this section, the models used to help interpret the results of this
627 thesis will be discussed. All of these models are capable of simulating pp, p–Pb, and
628 Pb–Pb events.

629 1.7.1 PHSD

630 Parton-Hadron-String-Dynamics (PHSD) [92], [93] is the only model explored in this
631 thesis that utilizes a **microscopic transport approach**: it simulates the full space-
632 time evolution of a heavy-ion collision by modeling the interactions of individual
633 particles. Here “particles” refers to different quantities (strings, partons, hadrons)
634 which are all evolved in different ways. The transport equations of the partons and
635 hadrons are derived from the Kadanoff-Baym (KB) equations [94], which describe
636 the non-perturbative transport of particles in a strongly interacting system. The
637 evolution of a collision within PHSD is as follows.

638 1.7.1.1 Initial stages

639 Prior to the collision, the simulation is broken up into a 3D-grid of size 56 in each
640 of the x, y, and z directions. The total size of the grid increases with each time step
641 such that the number of particles within a given cell evolves smoothly with time. The
642 initial momentum distribution and abundances of partons within the nuclei (prior to
643 any collision) are given by the thermal distributions

$$f(\omega, \vec{p}) = C_i p^2 \omega \rho_i(\omega, \vec{p}) n_{F/B}(\omega/\tau), \quad (1.12)$$

644 where ρ_i are the spectral functions of the quarks and gluons ($i = q, \bar{q}, g$) and $n_{F/B}$ are
645 the Fermi-Dirac (for quarks) and Bose-Einstein (for gluons) distributions. Once the
646 nuclei collide, the partons interact with each other under the Lund string model to
647 form *leading hadrons* (at large rapidity) and *pre-hadrons* (at midrapidity), as shown

648 in Figure 1.17. The leading hadrons are immune to dissociation within the QGP,
 649 while the pre-hadrons are not.

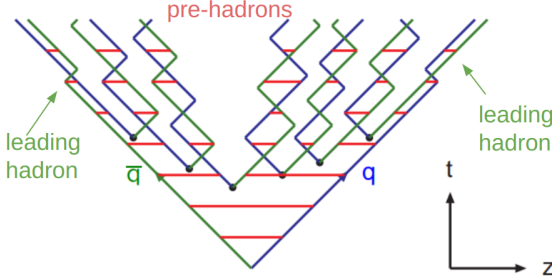


Figure 1.17: The Lund string model, with pre-hadrons and leading hadrons labeled.

650 1.7.1.2 QGP phase

651 If the energy density ϵ of a given cell increases beyond the critical energy density
 652 $\epsilon_c = 0.5 \text{ GeV/fm}^3$, the pre-hadrons within that cell are dissolved into partons. The
 653 partons are then treated as interacting quasi-particles under the DQPM [95] model,
 654 with Lorentzian spectral functions given by

$$\rho_j(\omega) = \frac{\gamma_j}{E_j} \left(\frac{1}{(\omega - E_j)^2 + \gamma_j^2} - \frac{1}{(\omega + E_j)^2 + \gamma_j^2} \right) \quad (1.13)$$

655 where i is one of (q, \bar{q}, g) and the width γ_i is given by

$$\gamma_g(T) = N_c \frac{g^2 T}{8\pi} \ln \frac{2c}{g^2}, \quad \gamma_q(T) = \frac{N_c^2 - 1}{2N_c} \frac{g^2 T}{8\pi} \ln \frac{2c}{g^2}, \quad (1.14)$$

656 where T is the temperature (calculated from the energy density within a given cell).
 657 This is the key difference between DQPM and other transport models—the quarks and
 658 gluons have non-zero temperature-dependent widths in the medium! The coupling
 659 constant g is also temperature dependent, and is of the form

$$g^2(T/T_c) = \frac{48\pi^2}{(11N_c - 2N_f) \ln (\lambda^2 (T/T_c - T_s/T_c)^2)}. \quad (1.15)$$

660 The parameters T_s and λ are fit to lattice QCD (lQCD) results [93]. The spectral
 661 functions are enough to describe the propagation of the mean-fields of the partons
 662 (effectively their Greens functions) via the aforementioned KB equations. The col-
 663 lisional terms in these equations are determined by the modified scattering cross

664 sections of the partons. These cross sections are calculated using the leading order
 665 Feynman diagrams, with the DQPM-modified quark and gluon propagators given by

$$i\delta_{ij} \frac{q + M_q}{q^2 - M_q^2 + 2i\gamma_q q_0} \quad (1.16)$$

666 and

$$-i\delta_{ab} \frac{g^{\mu\nu} - q^\mu q^\nu / M_g^2}{q^2 - M_g^2 + 2i\gamma_g q_0}, \quad (1.17)$$

667 respectively. Due to the large masses of the gluons, $q + \bar{q} \rightarrow g + g$ and $g \rightarrow g + g$ are
 668 suppressed and thus not included in the model.

669 1.7.1.3 Hadronization

670 Whenever the energy density of a given cell falls below the aforementioned critical
 671 energy density ($\epsilon_c = 0.5$ GeV/fm³), the partons within begin to hadronize. The
 672 dynamical hadronization of partons into hadrons is modeled by the equations

$$\begin{aligned} \frac{dN_m(x, p)}{d^4x d^4p} &= \text{Tr}_q \text{Tr}_{\bar{q}} \delta^4(p - p_q - p_{\bar{q}}) \delta^4\left(\frac{x_q + x_{\bar{q}}}{2} - x\right) \\ &\times \omega_q \rho_q(p_q) \omega_{\bar{q}} \rho_{\bar{q}}(p_{\bar{q}}) |v_{q\bar{q}}|^2 W_m(x_q - x_{\bar{q}}, (p_q - p_{\bar{q}})/2) \\ &\times N_q(x_q, p_q) N_{\bar{q}}(x_{\bar{q}}, p_{\bar{q}}) \delta(\text{flavor, color}). \end{aligned} \quad (1.18)$$

673 for mesons and

$$\begin{aligned} \frac{dN_B(x, p)}{d^4x d^4p} &= \text{Tr}_{q_1} \text{Tr}_{q_2} \text{Tr}_{q_3} \delta^4(p - p_{\xi_3}) \delta^4(x - \xi_3) \delta\left(\sqrt{(\tau_1 - \tau_2)^2}\right) \\ &\times \omega_{q_1} \rho_{q_1}(p_1) \omega_{q_2} \rho_{q_2}(p_2) \omega_{q_3} \rho_{q_3}(p_3) \\ &\times |M_{qqq}|^2 W_B(\xi_1, \xi_2, p_{\xi_1}, p_{\xi_2}) \\ &\times N_{q_1}(x_1, p_1) N_{q_2}(x_2, p_2) N_{q_3}(x_3, p_3) \delta(\text{flavor, color}). \end{aligned} \quad (1.19)$$

674 for baryons. The terms for the meson case are described as follows:

- 675 • Tr_q is shorthand notation for $\text{Tr}_q = \sum_q \int d^4x_q \int \frac{d^4p_q}{(2\pi)^4}$, where q is summed over
 676 all spin, color, and flavor degrees of freedom.
- 677 • $\delta^4(p - p_q - p_{\bar{q}})$ forces conservation of four-momentum. Note that the quarks
 678 and anti-quarks are allowed to be off-shell (due to their non-zero widths), thus
 679 this can result in off-shell mesons.

- 680 • $\delta^4\left(\frac{x_q+x_{\bar{q}}}{2} - x\right)$ puts the resulting meson in-between the quark and anti-quark
 681 pair.
- 682 • ω_q and $\omega_{\bar{q}}$ are the energies of the quark and anti-quark, respectively.
- 683 • $\rho_q(p_q)$ and $\rho_{\bar{q}}(p_{\bar{q}})$ are the aforementioned spectral functions of the quark and
 684 anti-quark, respectively.
- 685 • $|v_{q\bar{q}}|^2$ is the DQPM-determined *effective quark-anti-quark interaction*, which is
 686 shown as the green dashed line in Figure 1.18. Note that this value is very small
 687 for large quark (energy) densities, and thus this entire equation is effectively
 688 zero. However, for low quark densities this value blows up, which “turns on” the
 689 hadronization (and also guarantees that all partons will hadronize *eventually*).
- 690 • $W_m(x_q - x_{\bar{q}}, (p_q - p_{\bar{q}})/2)$ is the phase-space distribution of the resulting (pre-
 691)meson
- 692 • $N_q(x_q, p_q)$ and $N_{\bar{q}}(x_{\bar{q}}, p_{\bar{q}})$ are the phase-space densities of the quark and anti-
 693 quark, respectively.
- 694 • $\delta(\text{ flavor, color })$ is shorthand for “make sure flavor quantum numbers are con-
 695 served and that the resulting meson is color-neutral”.

696 The terms for the baryon case are similar.

697 The numerical integrations of equations 1.18 and 1.19 for a fixed test parton
 698 ultimately give the probability for a hadronization event to occur. From there, events
 699 are randomly selected using Monte Carlo techniques, which give a color neutral state
 700 with definite x, p and flavor. However, this is *still* not enough to specify a hadron
 701 completely: many hadronic states of the same flavor have large widths. Thus to
 702 determine the identity of the final hadron, the weight of each possible²⁰ hadronic
 703 spectral function is computed. The hadron is then randomly assigned an identity
 704 based on these weights using Monte Carlo.

²⁰PHSD only includes the baryon octet/decouplet, the spin 0 and spin 1 meson nonets, and a few higher resonance states. Furthermore, if the invariant mass of the color neutral state is above 1.3 GeV (for mesons) or 1.5 GeV (for baryons), the state is treated as a Lund string with further decay handled by the JETSET algorithm [96]

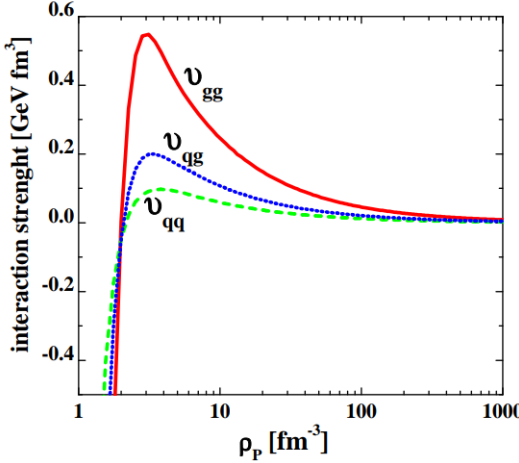


Figure 1.18: The effective quark-quark (green), quark-gluon (blue), and gluon-gluon (red) interactions as a function of parton density in DQPM, taken from [92].

705 1.7.1.4 Hadronic phase

706 All of the hadrons produced in the previous steps are transported using Hadron-
 707 String-Dynamics [97] (PHSD without the P). The phase-space distributions of the
 708 hadrons in HSD are transported using the equation

$$\begin{aligned} & \left\{ \left(\Pi_\mu - \Pi_\nu \partial_\mu^p U_h^\nu - M_h^* \partial_\mu^p U_h^S \right) \partial_x^\mu + \left(\Pi_\nu \partial_\mu^x U_h^\nu + M_h^* \partial_\mu^x U_h^S \right) \partial_p^\mu \right\} f_h(x, p) \\ &= \sum_{h_2 h_3 h_4 \dots} \int d2d3d4 \dots [G^\dagger G]_{12 \rightarrow 34\dots} \delta_\Gamma^4(\Pi + \Pi_2 - \Pi_3 - \Pi_4 \dots) \\ & \quad \times \left\{ f_{h_3}(x, p_3) f_{h_4}(x, p_4) \bar{f}_h(x, p) \bar{f}_{h_2}(x, p_2) \right. \\ & \quad \left. - f_h(x, p) f_{h_2}(x, p_2) \bar{f}_{h_3}(x, p_3) \bar{f}_{h_4}(x, p_4) \right\} \dots, \end{aligned} \quad (1.20)$$

709 where U_h^S and U_h^μ are the scalar and vector hadron self-energies, respectively. The
 710 effective mass of the hadron M_h^* is given by

$$M_h^* = M_h + U_h^S, \quad (1.21)$$

711 and its effective momentum is given by

$$\Pi^\mu = p^\mu - U_h^\mu. \quad (1.22)$$

712 The ‘‘collisional’’ term $[G^\dagger G]_{12 \rightarrow 34\dots}$ is the transition rate for the process $1 + 2 \rightarrow$
 713 $3 + 4 + \dots$, which is modeled using Lund string fragmentation. The self-energies U_h^S

714 and U_h^μ are evaluated on the basis of a Nambu-Jona-Lasinio (NJL)-type model [98]
715 for the QCD Lagrangian. Once these self-energies (and $[G^\dagger G]_{12 \rightarrow 34\dots}$) are specified,
716 the transport equation (Equation 1.20) can be solved.

717 1.7.1.5 A simple overview

718 While the equations that govern PHSD are quite complicated, the overall picture is
719 relatively simple. It can be summarized as follows:

- 720 • First, the simulation is split up into cells whose sizes evolve with time, as shown
721 in Figure 1.19.
- 722 • As the initial nuclei collide, and the interacting partons form pre-hadrons and
723 leading hadrons.
- 724 • If the energy density of a cell is too high, the pre-hadrons dissolve into partons,
725 which are handled by the DQPM model.
- 726 • If a cell with partons in it cools off, the partons dynamically hadronize.
- 727 • The resulting hadrons (and any hadrons present in a particular cell) are trans-
728 ported using HSD.

729 1.7.2 EPOS LHC

730 In the EPOS LHC [99] model, the initial colliding nuclei results in many parton-
731 parton scatterings happening in parallel, as shown in Figure 1.20. These simultaneous
732 scatterings form a parton ladder, which are modeled as relativistic Lund strings. Long
733 before hadronization, the model separates into two distinct parts: the *core* and the
734 *corona*. This designation is based on the string density (i.e. the number of string
735 segments per unit volume). If the string density exceeds a critical density ρ_c , the
736 string segments are considered to be in the core. Otherwise, they are in the corona.

737 The core is evolved in a hydrodynamic manner, which loses all information about
738 the initial string segments and their interactions. Hadronization in the core is handled
739 by a microcanonical procedure known as Cooper-Frye freeze-out, which is described
740 in detail in [100]. The core is associated with the QGP medium, and dominates
741 particle production at higher multiplicities. The corona, however, corresponds to

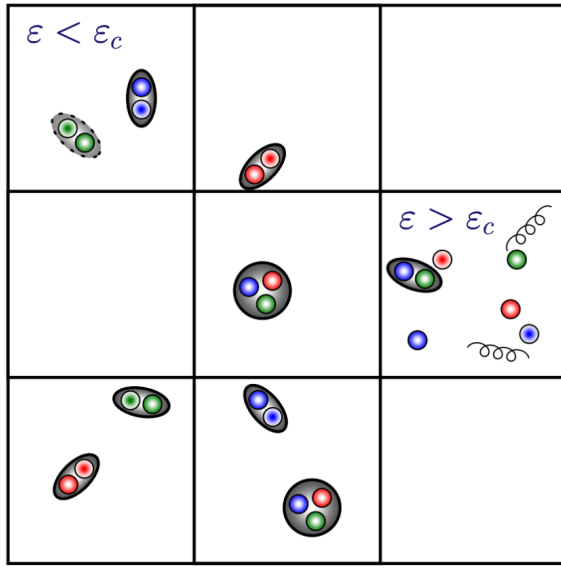


Figure 1.19: The cells within PHSD. If the energy density of the cell is greater than the critical energy density, the pre-hadrons dissolve into partons.

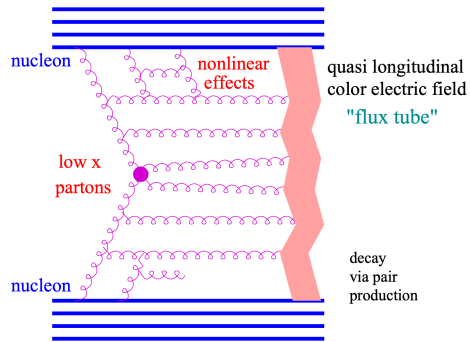


Figure 1.20: A schematic of the elementary interaction in EPOS LHC in which many parton-parton interactions are occurring simultaneously [99].

742 unmodified Lund string fragmentation, which dominates at large rapidity and in
 743 lower multiplicity events.

744 **1.7.3 DPMJET**

745 Perhaps the most simple²¹ event generator explored in this thesis is the DPMJET [101]
746 model. DPMJET combines the Dual Parton Model (DPM) [102] with the Lund string
747 model [59] to describe proton-proton, proton-nucleus, and nucleus-nucleus collisions
748 across a large range of energies. The DPM describes all of the soft, non-perturbative
749 multi-particle events that occur within a heavy ion collision using various large N_c
750 and N_f limits of QCD. This is the only model explored in this thesis that does
751 not have an explicit QGP phase, as the collision constituents²² are always treated
752 independently. Thus DPMJET serves as a good baseline for vacuum fragmentation,
753 and can be compared with other models (and data) to help quantify the effects of the
754 explicit QGP phase.

²¹Still *extremely* complicated from a theoretical perspective, but has the least moving parts.

²²Strings. It's always strings.

Chapter Two: Summary and outlook

756 Quantum chromodynamics (QCD) is the theory that describes how the protons and
757 neutrons, which compose almost all ordinary matter, are bound to one another within
758 the nucleus of an atom. In this theory, the fundamental constituents of matter are
759 *not* protons and neutrons, but rather quarks and gluons. These quarks and gluons
760 bind together through their color charge, creating the color neutral hadrons observed
761 in nature. One of the most interesting predictions of QCD is that, at extreme temper-
762 atures and densities, these hadrons dissolve into their constituent quarks and gluons,
763 forming a new state of matter known as the Quark-Gluon Plasma (QGP). Under-
764 standing the QGP, which is thought to be the state of the universe shortly after the
765 Big Bang, can help answer questions about the nature of everyday matter and the
766 evolution of the universe.

767 Studying the QGP requires recreating the extreme conditions of the early uni-
768 verse, which can only be achieved through high energy particle collisions. In such
769 collisions, however, the QGP is only produced for a very short time, after which it
770 expands and cools into the hadrons that are observed in the detector. Thus the QGP
771 cannot be studied directly, and its formation and properties must be inferred from
772 the information that is accessible to experiment. One of the first predicted exper-
773 imental signatures for the formation of this plasma is the enhancement of strange
774 hadron production, relative to non-strange pion production. While this enhancement
775 was thought to be unique to heavy-ion collisions, experimental data from ALICE
776 indicates that even high multiplicity pp and p–Pb collisions exhibit an onset of this
777 enhanced production. This enhancement can only be described using statistical mod-
778 els, as its microscopic origin is not yet understood.

779 One way to study the strange particles that are produced in these high energy
780 collisions is through jets, which are sprays of hadrons that come from a hard inter-
781 action of the partons inside the nuclei. By looking at how a high-momentum hadron
782 (that represents a jet direction) and a lower momentum strange hadron are aligned
783 in azimuthal angle, it is possible to separate the processes that create strangeness
784 between hard (jet-related) and soft (QGP-related) ones. This angular correlation
785 method can be used to further the understanding of how strangeness production de-

786 pends on the multiplicity in these different regimes, thus providing insight to the
787 onset of strangeness enhancement in smaller collision systems.

788 This thesis presents the first results using angular correlations to measure jet and
789 non-jet Λ and charged hadron production in p–Pb collisions at $\sqrt{s_{\text{NN}}} = 5.02$ TeV. By
790 using the technique of two-particle angular correlations, the production of Λ baryons
791 can be separated into different kinematic regions: the near-side region (associated
792 with jet-like strangeness production without QGP modification) away-side region
793 (associated with jet-like production in the presence of the QGP), and the underlying
794 event (tied to the uncorrelated strangeness production in the QGP). Both the yields
795 and the jet widths on the near- and away-side regions are extracted from the azimuthal
796 correlation functions and studied as a function of associated momentum and event
797 multiplicity. A strong dependence on multiplicity is observed for both the near-
798 and away-side yields in the case of the Λ , whereas the charged hadron associated
799 yields exhibit a much smaller (nearly statistically insignificant) dependence. The
800 away-side yields also show a systematically larger increase with multiplicity than the
801 near-side yields for both cases, hinting at modification of the away-side production
802 due to jet-QGP interactions. The h- Λ and h-h near-side jet widths reveal a large
803 dependence on p_{T} , becoming more collimated as momentum increases. The widths of
804 the away-side jets are found to be independent of both p_{T} and multiplicity, however
805 the larger systematic uncertainties introduce difficulties with excluding flat behavior.
806 Comparing width values of the h- Λ and h-h correlations, the h- Λ near-side widths
807 are found to be significantly ($> 2\sigma$) larger than the dihadron widths, whereas the
808 away-side widths are consistent within uncertainties. This indicates that Λ baryons
809 are more readily produced in the peripheral regions of the jet cone, whereas charged
810 hadrons are produced closer to the jet axis. This hints at a modification of the jet
811 fragmentation process for strange hadrons, as more massive particles (like the Λ) are
812 expected to be produced closer to the jet axis.

813 The yield ratios $R_i^{\Lambda/h}$ and $R_i^{\Lambda/\phi}$ ($i = \text{near-side jet, away-side jet, UE}$) are also
814 studied as a function of associated p_{T} and multiplicity. The Λ/h ratios exhibit a clear
815 ordering in each region for the entire multiplicity range in both p_{T} bins, with the
816 UE ratios being larger than the away-side ratios, which are larger than the near-side
817 ratios. This indicates that relative Λ production is larger in the UE (QGP) when
818 compared to the jet-like regions. The Λ/h ratios in each region also reveal a strong
819 dependence on multiplicity, with slopes that are greater than zero by nearly 5σ for

820 both momentum bins. This indicates that while the overall Λ production is mostly
821 concentrated in the UE, the observed enhancement of Λ production with increasing
822 multiplicity is *also* driven by the jet-like regions. Furthermore, the away-side slopes
823 are found to be systematically higher than the near-side slopes, indicating that the
824 away-side Λ production is more strongly enhanced than the near-side Λ production
825 with increasing multiplicity. Again, this suggests that the away-side jet strangeness
826 production is modified by medium interactions. The Λ/ϕ ratios in the near-side jet
827 region are measured to be systematically higher than both the away-side and UE
828 ratios, hinting at a suppression of ϕ mesons along the jet axis due to the lack of
829 available s -quarks in the unmodified jet. The slopes of these ratios in all kinematic
830 regions are consistent with zero, indicating that the ratio is independent of collision
831 centrality.

832 The measurements in this thesis are compared with theoretical predictions from
833 the PHSD, EPOS and DPMJET models. PHSD is found to be in good agreement with
834 all dihadron measurements, but fails to describe the overall Λ yields. This is likely
835 due to the requirement of a high momentum trigger hadron, which are not readily
836 produced within the model. Even still, the shape of the near-side peak in the h- Λ
837 correlation distribution is well-described by PHSD. EPOS, on the otherhand, is able
838 to describe the Λ and hadron yields very well, but the correlation distributions are
839 dominated by elliptic flow, making it impossible to extract the jet-like components.
840 This flow contribution is much larger for the h- Λ distributions, indicating that Λ
841 baryons in EPOS are mostly produced within the hydronamic core. The predicted
842 near- and away-side yields from DPMJET are found to be in relatively good agreement
843 with data in the dihadron case, but the h- Λ yield predictions deviate from data by a
844 large ($> 40\%$) margin. DPMJET also fails to predict any of the observed multiplicity
845 dependence for both the h- Λ and h-h jet yields. However, the model is able to closely
846 predict the near-side widths of the dihadron distributions across all multiplicity and
847 momentum ranges, although it underpredicts both the h- Λ near-side widths and
848 the away-side widths for both (Λ , h) cases. The model also predicts a difference
849 between the h- Λ and h-h near-side widths, which is observed in data as well. This
850 indicates that whatever process responsible for the production of strangeness in the
851 periphery of the jet cone is contained within DPMJET. The per-trigger Λ/h and Λ/ϕ
852 yield ratios are consistently underpredicted by DPMJET, and exhibit no multiplicity
853 dependence. Even still, DPMJET manages to predict the ordering of the Λ/h ratios

854 in each region (UE > away-side jet > near-side jet) and the enhancement of the
855 jet-like Λ/ϕ ratio when compared to the UE region. Thus the softer, uncorrelated
856 processes implemented in DPMJET are responsible for the majority of the relative
857 strangeness production.

858 2.1 Future outlook

859 The measurements presented in this thesis strongly indicate that, while the dom-
860 inating component for strangeness production comes from the QGP, the observed
861 *enhancement* of this production as a function of multiplicity has a large contribution
862 from the jet-like regions. More still, the away-side jet component appears to undergo
863 a larger enhancement than the near-side, hinting that the jet and medium are inter-
864 acting in such a way that strangeness is more readily produced. These observations
865 can be used to help fuel the theoretical models used to describe particle collisions, as
866 such models are currently incapable of describing these results in their entirety.

867 The techniques presented in this thesis can be easily extended to other collision
868 systems, such as pp and Pb–Pb collisions, along with other particle species, such as
869 the K^0 . With the advent of the Run 3 data-taking period at the LHC, the ALICE
870 detector will be able to collect more data than ever before, allowing for more precise
871 measurements of these observables across a wider range of particles and collision
872 systems. Such measurements will help further constrain the microscopic origins of
873 this strange enhancement, thus providing more insight into the nature of the QGP
874 and the universe as a whole.

875

Appendix A: Resonance technique for Λ reconstruction

876

877

A.1 Introduction

This portion of the appendix is dedicated to describing the analysis procedure for generating the $h-\Lambda$ correlation distributions using lambdas which are reconstructed using the **resonance technique**, where all proton-pion pairs in an event are combined to form Λ candidates. All of the proton and pion daughter tracks meet the same selection criteria as the tracks used in the V^0 technique, described in Table ???. All in all, the procedure is very similar to the one described in Chapter ??, but with a few key differences that will be highlighted in the following sections.

885

A.2 Combinatorial background estimation

As Λ baryons reconstructed using the resonance technique will have a much larger combinatorial background than those from the nominal procedure, the final correlation will contain a higher fraction of $h-(p\pi)$ pairs that need to be removed. While the sideband subtraction technique provides a general procedure for removing these pairs, the signal S and the background B of the Λ invariant mass distribution must be well described. To estimate these quantities, the following techniques were explored:

892

- **Like-sign $p\pi$ pairs** - Reconstruct the invariant mass of like-sign (LS) $p\pi$ pairs, and scale the like-sign $p\pi$ distribution to the unlike-sign (US) $p\pi$ distribution in a region outside of the Λ signal region.

895

- **Rotated $p\pi$ pairs** - Reconstruct the invariant mass of US $p\pi$ pairs, but rotate either the pion or proton around the z-axis by π radians, and scale the rotated $p\pi$ distribution to the original US sign $p\pi$ distribution in a region outside of the Λ signal region.

- 899 • **Voigtian + polynomial fit** - Perform a standard fitting procedure using a
 900 Voigtian distribution for the signal along with a second-order polynomial for
 901 the background.

902 The last technique will be addressed first, as it fails to properly estimate the signal
 903 and background in data. To illustrate this, the best possible fits in data are found
 904 and the corresponding signal shape is extracted and compared with the signal shape
 905 in Monte Carlo using full track reconstruction via GEANT. This comparison is done
 906 for the 20-50% multiplicity bin in Figure A.1. Note that the background shown in the
 907 MC plot is the true combinatorial background, as the $p\pi$ pairs are accessed directly
 908 at the generator level to confirm they did not come from a Λ decay.

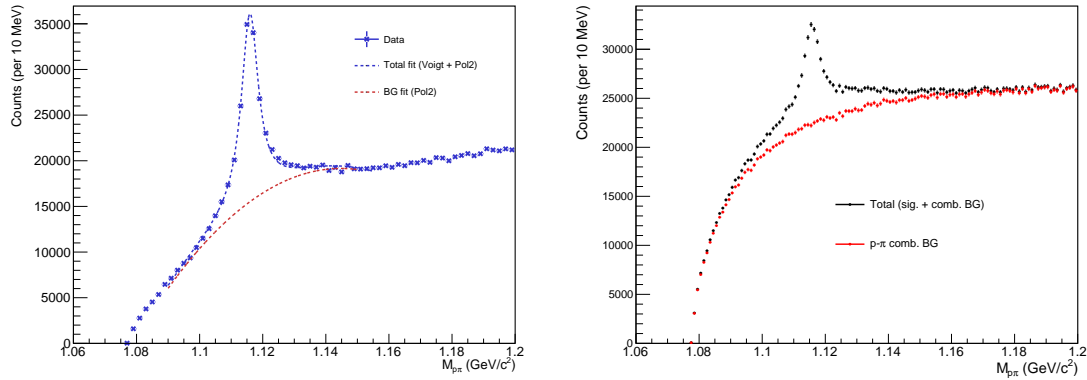


Figure A.1: Left: Invariant mass distribution with corresponding Voigt + Polynomial fit in the 20-50% multiplicity bin (data). Right: The signal and background shapes in MonteCarlo (MC). Note that even though MC appears to have a completely different S/B, the signal shapes should be similar. The fit in data appears to be massively underestimating the Λ signal, as the MC sample indicates there is Λ signal where the total data fit converges with the BG fit.

909 This plot shows the main issue with reconstructing Λ baryons using the resonance
 910 technique: the tails of the signal distribution are much wider than the signal distri-
 911 bution obtained using the V^0 method. This is due to the fact that the kinematics
 912 of the corresponding daughter tracks are calculated assuming they originated from
 913 the primary vertex, which is only approximately true in the cases where the Λ is
 914 short-lived. This is different than the V^0 method, which calculates the kinematics for
 915 the daughter tracks assuming they originated from the secondary vertex. The wider
 916 tails of the distribution make it extremely difficult to describe using any common

917 distribution, thus all techniques that rely on fitting the signal shape are not viable.
 918 Because of this, only the first two techniques (like-sign and rotated p π pairs) will be
 919 considered for the rest of this analysis.

920 To determine which of the two remaining techniques is more effective, the back-
 921 ground shape of the Λ invariant mass distribution for both techniques in MonteCarlo
 922 is compared to the ground-truth background shape. The resulting invariant mass
 923 distributions from like-sign and rotated p π pairs are shown in Figure A.2, along with
 924 a comparison of the extracted signal shapes. The LS and rotated p π distributions are
 925 scaled to match the US distribution in the sideband region, which will be discussed
 926 in the next section. The LS p π pairs match the background shape of the Λ invariant
 927 mass distribution more closely than the rotated p π pairs, so they are used to estimate
 928 the combinatorial background in the Λ invariant mass distribution in data.

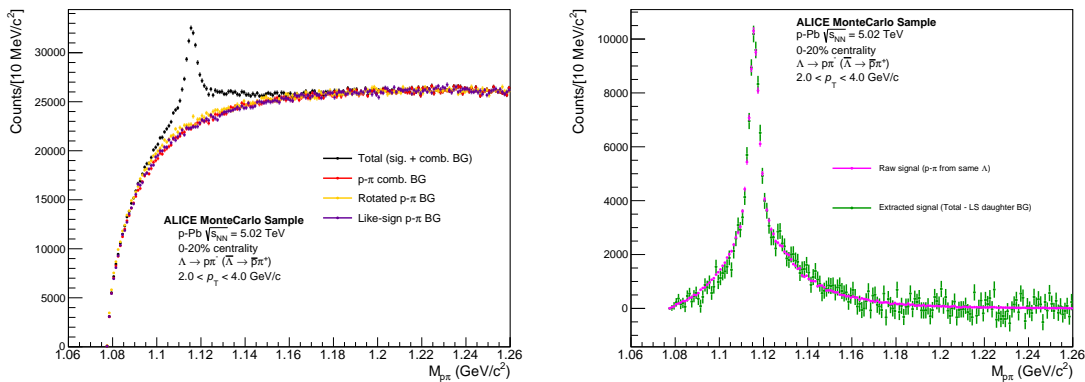


Figure A.2: Left: Invariant mass distribution for reconstructed unlike-sign p π pairs (black) in the MonteCarlo sample. The like-sign p π pair mass distribution (purple) and unlike-sign rotated p π distributions are scaled to match the unlike-sign distribution outside of the Λ signal range. The true combinatorial background (red) matches most closely with the like-sign pairs. Right: The actual Λ signal (magenta) compared with the result of subtracting the like-sign from the total unlike-sign p π distribution (green). The two distributions show good agreement.

929 A.3 Signal and sideband regions

930 As the invariant mass distributions from lambdas reconstructed using the resonance
 931 technique are very different from those reconstructed using the V⁰ technique, so

932 too must the signal and sideband regions be different. The signal region was again
 933 chosen to maximize significance across all multiplicity bins, and is defined as the range
 934 $1.014 < M_{p\pi} < 1.026 \text{ GeV}/c^2$. Choosing the sideband region is a more complicated
 935 procedure, as there is no obvious region in the invariant mass distribution where the
 936 signal vanishes. Instead, the sideband region is chosen to minimize the difference
 937 between the extracted signal in data and the signal shape in MonteCarlo, which can
 938 be seen in Figure A.3. The resulting sideband region is $1.160 < M_{p\pi} < 1.180 \text{ GeV}/c^2$.

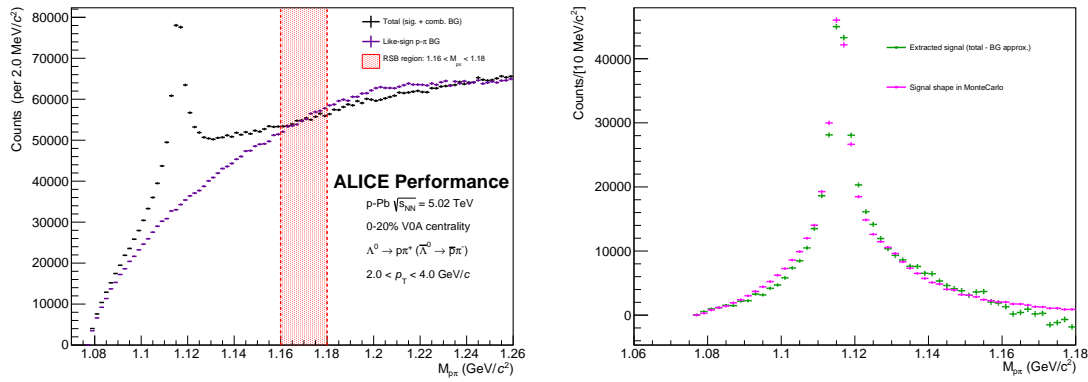


Figure A.3: Left: Invariant Mass distribution for unlike-sign $p\pi$ pairs (black) along with the like-sign $p\pi$ background (purple) and the sideband region (red) in the 0-20% multiplicity bin. Right: The extracted signal (green) compared with the resonance-technique reconstructed signal shape in MonteCarlo (magenta). The sideband region was chosen to minimize the differences between these distributions.

939 A.3.1 Efficiency correction

940 Again, the resonance technique-based Λ reconstruction efficiency is calculated in a
 941 similar manner as the V^0 technique, using the formula

$$\epsilon(x_1, x_2, \dots, x_n) = \frac{N_{\text{reco.}}(x_1, x_2, \dots, x_n)}{N_{\text{gen.}}(x_1, x_2, \dots, x_n)}, \quad (\text{A.1})$$

942 where $N_{\text{reco.}}$ and $N_{\text{gen.}}$ are the reconstructed and generated particle distributions with
 943 kinematic variables x_1, x_2, \dots, x_n . The main difference from the V^0 efficiency computa-
 944 tion comes from $N_{\text{reco.}}$, where each Λ candidate is generated using the following
 945 procedure:

- 946 • Find all protons and pions within the track list that pass the daughter selection
 947 criteria

- 948 • For each proton in the list, determine if it came from a Λ (at generator level)
- 949 • If the proton came from a Λ , loop through the pion list until the pion that came
- 950 from the same Λ is found (again, verified at the generator level)
- 951 • Reconstruct the Λ using the daughter tracks found in the previous two steps
- 952 • Only keep the Λ if $|\eta| < 0.8$

953 The denominator $N_{\text{gen.}}$ is calculated in the same way as the V^0 technique. The
 954 resulting efficiency is shown as a function of p_T for each multiplicity bin in Figure A.4.
 955 As expected, the efficiency is higher than the V^0 technique, as every Λ reconstructed
 956 using the resonance technique would also be reconstructed using the V^0 technique.

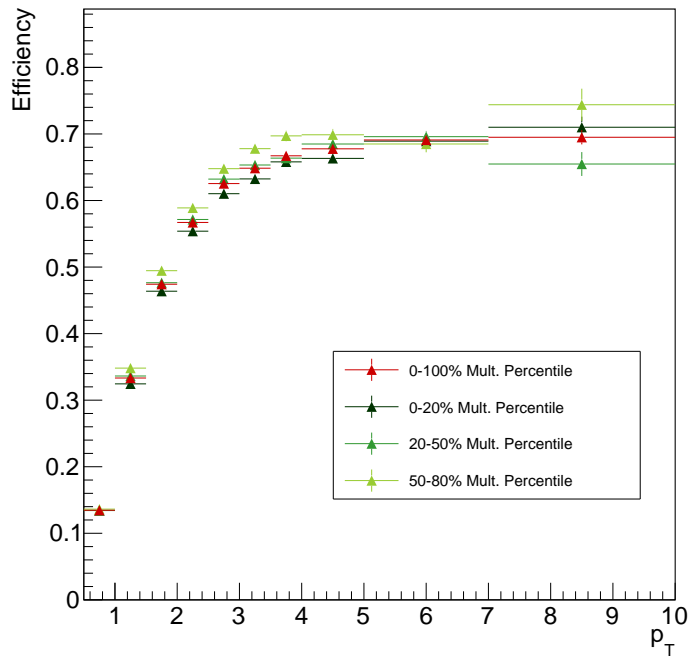


Figure A.4: Efficiency vs. p_T for Λ reconstruction using resonance technique for each multiplicity bin, along with an integrated 0-100% point in red. There does not appear to be any significant dependence on multiplicity. Also worth noting that the efficiency is higher for this technique when compared to the V^0 technique, as expected (all AOD tracks from V^0 finder daughters are also in total AOD track list).

957 **A.4 Corrections to the h- Λ distributions**

958 All of the efficiency and acceptance corrections are applied to the resonance technique-
 959 based h- Λ distribution in the same way as the V⁰ technique. The only difference comes
 960 from the removal of the combinatorial background, as:

- 961 1. The signal S and background B are calculated in a slightly different manner,
 962 and
- 963 2. The sideband region is vastly different.

964 For the first point, the signal and background are calculated via bin-wise summa-
 965 tion of the invariant mass distribution using the LS p π pairs as an estimate for the
 966 background, scaled to the US distribution in the sideband region.

967 The second point is mostly inconsequential as the h-p π distributions are very
 968 similar in a wide range of sideband regions, as shown in Figure A.5. The nominal
 969 sideband region was chosen to be $1.160 < M_{\text{SSB}} < 1.180 \text{ GeV}/c^2$, but any region with
 970 a lower bound greater than $1.160 \text{ GeV}/c^2$ and upper bound less than $1.22 \text{ GeV}/c^2$
 971 should produce similar results.

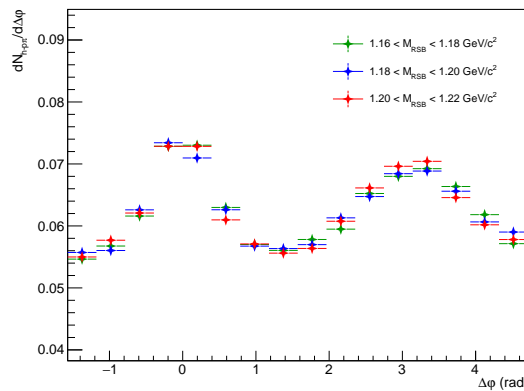


Figure A.5: The projected $\Delta\varphi$ distributions for different choices of sideband, taken within the $-1.2 < \Delta\eta < 1.2$ region. The correlation shapes are identical within the statistical errors.

972 The signal scaling factor is calculated in the same way as it is in Equation ??, but
 973 with the residual now generated by subtracting the sideband-scaled LS p π pairs from
 974 the US distribution. The two-track efficiency correction is not applied, as the tools

975 used to calculate the $\epsilon_{\text{pair}}(\Delta\varphi, \Delta\eta)$ template were not developed before the resonance
 976 technique-based analysis was completed.

977 A.5 MC closure test

978 An MC closure test was also performed for the resonance technique-based analysis,
 979 and the results are shown in Figure A.6. The ratio is consistent with unity, but the
 980 statistical fluctuations make it difficult to draw any meaningful conclusions.

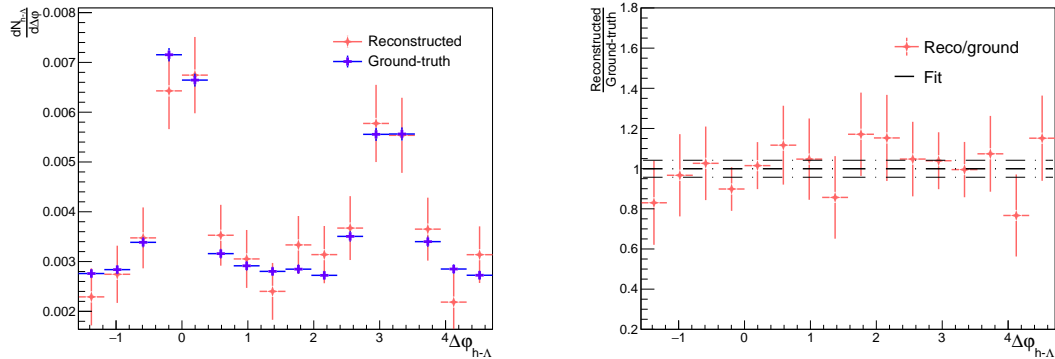


Figure A.6: The reconstructed (red) and ground-truth (blue) $h\text{-}\Lambda_{\text{res}}$ $\Delta\varphi$ distributions along with a (reconstructed)/(ground-truth) ratio and straight-line fit. The fit is technically consistent with unity, but the statistical fluctuations are quite large.

981 As the reconstructed distribution has not been corrected for the two-track merging
 982 effect, it is surprising that the ratio does not exhibit a significant deviation from unity
 983 at small $\Delta\varphi$. This is likely due to two factors:

- 984 1. The resonance technique has a much lower S/B, and therefore the sideband
 985 subtraction introduces a large amount of statistical fluctuations making such
 986 deviations difficult to observe, and
- 987 2. The reconstructed daughter tracks have a larger fraction of higher quality tracks
 988 when compared to the V^0 technique, and those tracks are less likely to be merged
 989 over by the trigger during reconstruction.

990 To elaborate on the second point, while the resonance and V^0 techniques use the
 991 same loose quality cuts, the daughter tracks coming from the V^0 technique must

992 have a resolvable secondary vertex, which biases the corresponding Λ sample to those
 993 with a higher decay length. As discussed in ??, the two-track merging effect is
 994 more pronounced at larger decay lengths, thus the $h\text{-}\Lambda$ distributions using the V^0
 995 reconstruction technique will have a larger fraction of merged tracks when compared
 996 to the resonance technique-based distributions.

997 To further investigate this surprising closure of the resonance technique-based $h\text{-}\Lambda$
 998 $\Delta\varphi$ distributions, the same closure test is performed, but for the reconstructed $h\text{-}\Lambda$
 999 distribution, the Λ candidate is required to have have a corresponding particle at the
 1000 generator-level, making the combinatorial background exactly zero and removing the
 1001 need for sideband subtraction. The results of this test are shown in Figure A.7. The
 1002 ratio is no longer consistent with unity at small $\Delta\varphi$, as expected¹

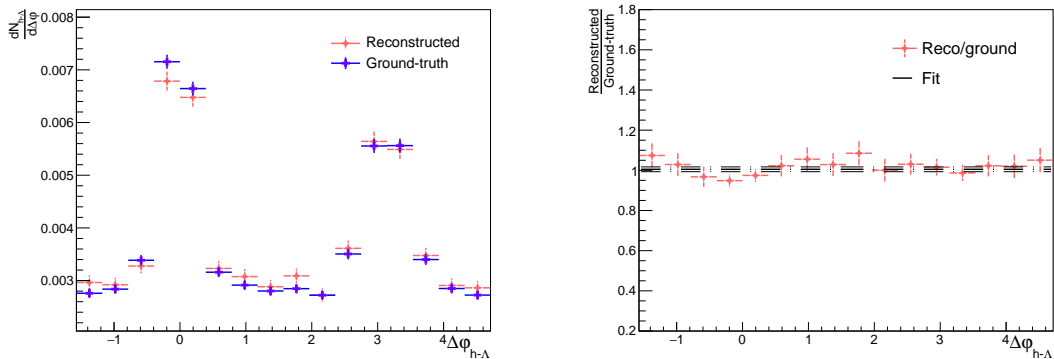


Figure A.7: The reconstructed (red) and ground-truth (blue) $h\text{-}\Lambda_{\text{res}}$ $\Delta\varphi$ distributions along with a (reconstructed)/(ground-truth) ratio and straight-line fit, but instead requiring the reconstructed Λ to have a corresponding particle at the generator level to make sideband subtraction unnecessary. The result is no longer consistent with unity at small $\Delta\varphi$ due to the track merging effect, but the non-closure is much smaller than the V^0 technique.

1003 A.6 Some additional results

1004 A comparison of the final per-trigger $h\text{-}\Lambda$ $\Delta\varphi$ correlation structure from the resonance
 1005 and V^0 -based techniques was shown in Chapter ??, but it can be seen again in

¹It is strange to *want* non-closure, but it would be even stranger if the track merging effect were somehow not present in the resonance technique-based analysis.

1006 Figure A.8. As mentioned previously, the correlation shapes are nearly identical, with
 1007 the resonance technique having slightly larger uncertainties due to the combinatorial
 1008 background subtraction.

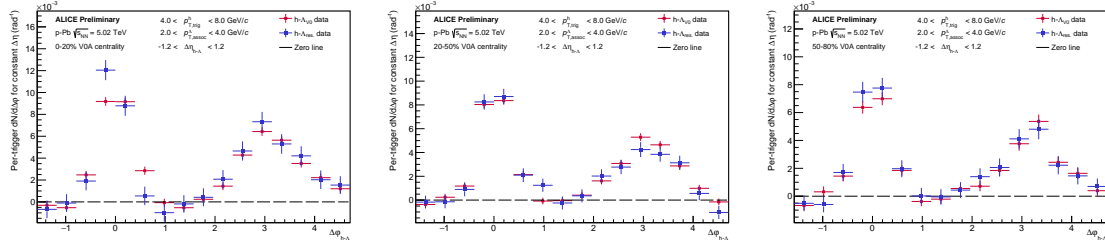


Figure A.8: The final per-trigger $h\text{-}\Lambda$ $\Delta\varphi$ correlations for Λ s reconstructed using the resonance technique (blue) and the V^0 -based technique (red) in the 0-20% (left), 20-50% (middle) and 50-80% (right) multiplicity bins, taken in the associated momentum range $2.0 < p_T < 4.0$ GeV/c, after the subtraction of the UE. The distributions show good agreement across all multiplicity bins, indicating that the V^0 -based reconstruction technique is not introducing a bias in the correlation shape.

1009 Additionally, the per-trigger near- and away-side pairwise yields and the $(h\text{-}\Lambda)/(h\text{-}h)$
 1010 ratios with Λ s reconstructed using the resonance technique are shown in Figure A.9.
 1011 The results are qualitatively very similar to the nominal results, indicating that the
 1012 resonance technique is a reasonably viable alternative to the V^0 technique. How-
 1013 ever, due to the larger combinatorial background (and likely very large systematic
 1014 uncertainties), the V^0 technique is still the preferred method for Λ reconstruction.

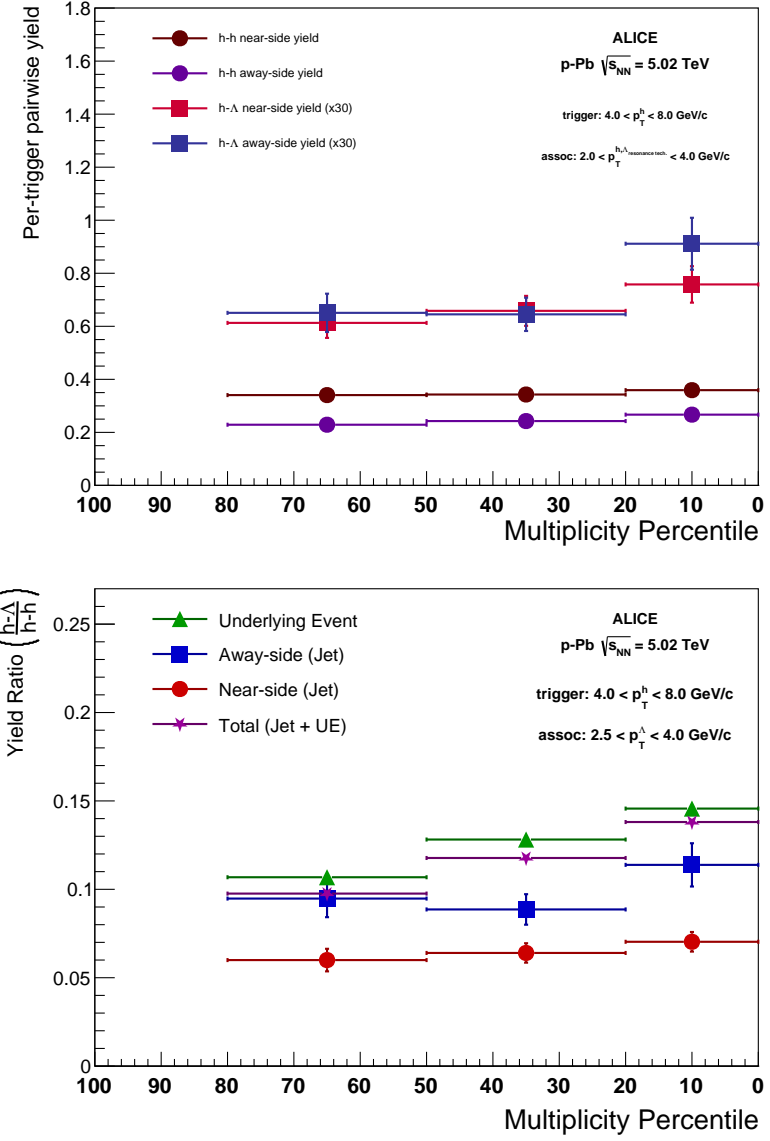


Figure A.9: The final $h\text{-}\Lambda$ and $h\text{-}h$ per-trigger pairwise jet yields (top) and $(h\text{-}\Lambda)/(h\text{-}h)$ yield ratios (bottom) vs. multiplicity in the associated momentum range $2.0 < p_T < 4.0 \text{ GeV}/c$ for Λ s reconstructed using the resonance technique. The general trends are similar to the nominal V^0 technique-based procedure, with larger statistical uncertainties.

Bibliography

- 1016 [1] B. Pullman, *The Atom in the History of Human Thought*. Oxford: Oxford
1017 University Press, 1998, ISBN: 978-0-19-515040-7 (cit. on p. 2).
- 1018 [2] J. Dalton, “Experimental enquiry into the proportion of the several gases
1019 or elastic fluids, constituting the atmosphere,” *Memoirs of the Literary and*
1020 *Philosophical Society of Manchester*, vol. 1, pp. 244–258, 1805 (cit. on p. 2).
- 1021 [3] E. R. Scerri, *The Periodic Table: A Very Short Introduction*. Oxford University
1022 Press, Jul. 2019, pp. 117–123, ISBN: 9780198842323. DOI: 10.1093/actrade/
1023 9780198842323.001.0001. [Online]. Available: <https://doi.org/10.1093/actrade/9780198842323.001.0001> (cit. on p. 2).
- 1025 [4] D. Mendeleev, “The natural system of elements and its application to the
1026 indication of the properties of undiscovered elements,” *Journal of the Russian*
1027 *Chemical Society*, vol. 3, pp. 25–56, 1871 (cit. on p. 2).
- 1028 [5] I. Falconer, “J J Thomson and the discovery of the electron,” *Physics Educa-*
1029 *tion*, vol. 32, no. 4, p. 226, 1997. DOI: 10.1088/0031-9120/32/4/015.
1030 [Online]. Available: <https://dx.doi.org/10.1088/0031-9120/32/4/015>
1031 (cit. on p. 3).
- 1032 [6] E. Rutherford, “The scattering of α and β particles by matter and the structure
1033 of the atom,” *Philosophical Magazine Series 6*, vol. 21, pp. 669–688, 1911 (cit.
1034 on p. 3).
- 1035 [7] J. Chadwick, “Possible existence of a neutron,” *Nature*, vol. 129, p. 312, 1932
1036 (cit. on p. 3).
- 1037 [8] C. D. Anderson, “The apparent existence of easily deflectable positives,” *Sci-*
1038 *ence*, vol. 76, no. 1967, pp. 238–239, 1932. DOI: 10.1126/science.76.1967.
1039 238. eprint: <https://www.science.org/doi/pdf/10.1126/science.76.1967.238>. [Online]. Available: <https://www.science.org/doi/abs/10.1126/science.76.1967.238> (cit. on p. 3).

- 1042 [9] S. H. Neddermeyer and C. D. Anderson, “Note on the nature of cosmic-ray
1043 particles,” *Phys. Rev.*, vol. 51, pp. 884–886, 10 1937. DOI: 10.1103/PhysRev.
1044 51.884. [Online]. Available: <https://link.aps.org/doi/10.1103/PhysRev.51.884> (cit. on p. 3).
- 1046 [10] R. Brown *et al.*, “Observations with Electron-Sensitive Plates Exposed to
1047 Cosmic Radiation,” *Nature*, vol. 163, no. 4133, pp. 82–87, Jan. 1949. DOI:
1048 10.1038/163082a0 (cit. on p. 3).
- 1049 [11] V. D. Hopper and S. Biswas, “Evidence concerning the existence of the new
1050 unstable elementary neutral particle,” *Phys. Rev.*, vol. 80, pp. 1099–1100, 6
1051 1950. DOI: 10.1103/PhysRev.80.1099. [Online]. Available: <https://link.aps.org/doi/10.1103/PhysRev.80.1099> (cit. on p. 3).
- 1053 [12] A. Barbaro-Galtieri *et al.*, “Apparent violation of the $\Delta S = \Delta Q$ rule by lep-
1054 tonic Σ^+ decay,” *Phys. Rev. Lett.*, vol. 9, pp. 26–29, 1 1962. DOI: 10.1103/
1055 PhysRevLett.9.26. [Online]. Available: <https://link.aps.org/doi/10.1103/PhysRevLett.9.26> (cit. on p. 3).
- 1057 [13] T. Nakano and K. Nishijima, “Charge Independence for V-particles,” *Progress
1058 of Theoretical Physics*, vol. 10, no. 5, pp. 581–582, 1953. DOI: 10.1143/PTP.
1059 10.581 (cit. on p. 3).
- 1060 [14] R. Serway, C. Moses, and C. Moyer, *Modern Physics*. Cengage Learning, 2004,
1061 pp. 12–13, ISBN: 9780534493394. [Online]. Available: <https://books.google.com/books?id=Yfo3rnt3bkEC> (cit. on p. 3).
- 1063 [15] M. Gell-Mann, “The Eightfold Way: A theory of strong interaction symmetry,”
1064 Mar. 1961. DOI: 10.2172/4008239. [Online]. Available: <https://www.osti.gov/biblio/4008239> (cit. on pp. 3, 4, 11).
- 1066 [16] Y. Ne’eman, “Derivation of strong interactions from a gauge invariance,” *Nu-
1067 clear Physics*, vol. 26, no. 2, pp. 222–229, 1961. DOI: 10.1016/0029-5582(61)
1068 90134-1 (cit. on p. 3).
- 1069 [17] W. Heisenberg, “Über den Bau der Atomkerne. I,” *Zeitschrift fur Physik*,
1070 vol. 77, no. 1-2, pp. 1–11, Jan. 1932. DOI: 10.1007/BF01342433 (cit. on
1071 p. 3).

- 1072 [18] M. Gell-Mann, “Isotopic Spin and New Unstable Particles,” *Physical Review*,
1073 vol. 92, no. 3, pp. 833–834, Nov. 1953. DOI: 10.1103/PhysRev.92.833 (cit. on
1074 pp. 3, 24, 28, 29).
- 1075 [19] T. Nakano and K. Nishijima, “Charge Independence for V-particles,” *Progress*
1076 *of Theoretical Physics*, vol. 10, no. 5, pp. 581–582, Nov. 1953. DOI: 10.1143/
1077 PTP.10.581 (cit. on p. 4).
- 1078 [20] M. Gell-Mann, “The interpretation of the new particles as displaced charge
1079 multiplets,” *Il Nuovo Cimento*, vol. 4, no. S2, pp. 848–866, Apr. 1956. DOI:
1080 10.1007/BF02748000 (cit. on p. 4).
- 1081 [21] M. Gell-Mann, “A schematic model of baryons and mesons,” *Physics Letters*,
1082 vol. 8, no. 3, pp. 214–215, Feb. 1964. DOI: 10.1016/S0031-9163(64)92001-3
1083 (cit. on p. 4).
- 1084 [22] A. Pickering, *Constructing quarks*. University of Chicago Press, 1999, pp. 114–
1085 125. DOI: 10.7208/chicago/9780226667997.003.0007 (cit. on p. 5).
- 1086 [23] B. J. Bjørken and S. L. Glashow, “Elementary particles and SU(4),” *Physics*
1087 *Letters*, vol. 11, no. 3, pp. 255–257, Aug. 1964. DOI: 10.1016/0031-9163(64)
1088 90433-0 (cit. on p. 5).
- 1089 [24] S. Glashow, “The hunting of the atoms and their nuclei: Protons and neu-
1090 trons,” *New York Times*, Jul. 1976. [Online]. Available: <https://www.nytimes.com/1976/07/18/archives/the-hunting-of-the-atoms-and-their-nuclei-protons-and-neutrons.html> (cit. on p. 5).
- 1093 [25] S. L. Glashow, J. Iliopoulos, and L. Maiani, “Weak Interactions with Lepton-
1094 Hadron Symmetry,” *Phys Rev D*, vol. 2, no. 7, pp. 1285–1292, Oct. 1970. DOI:
1095 10.1103/PhysRevD.2.1285 (cit. on p. 5).
- 1096 [26] H. Kendall, *Deep inelastic scattering: Experiments on the proton and the ob-
1097 servation of scaling*, 1990. [Online]. Available: <https://www.nobelprize.org/uploads/2018/06/kendall-lecture.pdf> (visited on 08/21/2023) (cit.
1098 on pp. 5, 6).
- 1100 [27] J. Friedman, *Deep inelastic scattering: Comparisons with the quark model*,
1101 1990. [Online]. Available: <https://www.nobelprize.org/uploads/2018/06/friedman-lecture.pdf> (visited on 08/21/2023) (cit. on p. 5).

- 1103 [28] R. Taylor, *Deep inelastic scattering: The early years*, 1990. [Online]. Available:
1104 <https://www.nobelprize.org/uploads/2018/06/taylor-lecture.pdf>
1105 (visited on 08/21/2023) (cit. on p. 5).
- 1106 [29] E. D. Bloom *et al.*, “High-Energy Inelastic e-p Scattering at 6° and 10° ,”
1107 *Physical Review Letters*, vol. 23, no. 16, pp. 930–934, Oct. 1969. DOI: 10.
1108 1103/PhysRevLett.23.930 (cit. on p. 5).
- 1109 [30] E. D. Bloom *et al.*, “High-Energy Inelastic e-p Scattering at 6° and 10° ,”
1110 *Physical Review Letters*, vol. 23, no. 16, pp. 930–934, Oct. 1969. DOI: 10.
1111 1103/PhysRevLett.23.930 (cit. on p. 5).
- 1112 [31] J. Bjorken, “Current algebra at small distances,” Jun. 2018. [Online]. Available:
1113 <https://www.osti.gov/biblio/1444446> (cit. on p. 6).
- 1114 [32] R. P. Feynman, “The behavior of hadron collisions at the uncertainties from
1115 these sources exhibit no multiplicity dependence, and a very small depen-
1116 dence on p_T . extreme energies,” in *Special Relativity and Quantum Theory:*
1117 *A Collection of Papers on the Poincaré Group*, M. E. Noz and Y. S. Kim,
1118 Eds. Dordrecht: Springer Netherlands, 1988, pp. 289–304, ISBN: 978-94-009-
1119 3051-3. DOI: 10.1007/978-94-009-3051-3_25. [Online]. Available: https://doi.org/10.1007/978-94-009-3051-3_25 (cit. on p. 6).
- 1120 [33] J. Aubert *et al.*, “Experimental observation of a heavy particle J ,” *Physical*
1121 *Review Letters*, vol. 33, Dec. 1974 (cit. on p. 6).
- 1122 [34] H. Fritzsch, M. Gell-Mann, and H. Leutwyler, “Advantages of the color octet
1123 gluon picture,” *Physics Letters B*, vol. 47, no. 4, pp. 365–368, Nov. 1973. DOI:
1124 10.1016/0370-2693(73)90625-4 (cit. on p. 7).
- 1125 [35] D. J. Gross and F. Wilczek, “Ultraviolet Behavior of Non-Abelian Gauge The-
1126 ories,” *Physical Review Letters*, vol. 30, no. 26, pp. 1343–1346, Jun. 1973. DOI:
1127 10.1103/PhysRevLett.30.1343 (cit. on p. 7).
- 1128 [36] H. D. Politzer, “Reliable Perturbative Results for Strong Interactions?” *Phys-
1129 ical Review Letters*, vol. 30, no. 26, pp. 1346–1349, Jun. 1973. DOI: 10.1103/
1130 PhysRevLett.30.1346 (cit. on p. 7).
- 1131 [37] P. Söding, *Twenty-five years of gluons*, 2004. [Online]. Available: <https://cerncourier.com/a/twenty-five-years-of-gluons/> (cit. on pp. 7, 13).

- 1134 [38] P. Söding, “On the discovery of the gluon,” *European Physical Journal H*,
1135 vol. 35, no. 1, pp. 3–28, Jul. 2010. DOI: 10.1140/epjh/e2010-00002-5 (cit.
1136 on p. 7).
- 1137 [39] A. Salam and J. C. Ward, “Weak and electromagnetic interactions,” *Il Nuovo
Cimento*, vol. 11, no. 4, pp. 568–577, Feb. 1959. DOI: 10.1007/BF02726525
(cit. on p. 7).
- 1140 [40] S. Weinberg, “A Model of Leptons,” *Physical Review Letters*, vol. 19, no. 21,
1141 pp. 1264–1266, Nov. 1967. DOI: 10.1103/PhysRevLett.19.1264 (cit. on p. 7).
- 1142 [41] P. W. Higgs, “Broken symmetries and the masses of gauge bosons,” *Phys. Rev.
Lett.*, vol. 13, pp. 508–509, 16 1964. DOI: 10.1103/PhysRevLett.13.508.
1143 [Online]. Available: <https://link.aps.org/doi/10.1103/PhysRevLett.13.508> (cit. on pp. 7–9).
- 1144 [42] P. T. Smith, “Reporting New Evidence of Gravitons,” in *14th International
Symposium on Nuclei in the Cosmos (NIC2016)*, S. Kubono *et al.*, Eds., Jan.
1145 2017, 020101, p. 020101. DOI: 10.7566/JPSCP.14.020101 (cit. on p. 7).
- 1146 [43] G. Jungman, M. Kamionkowski, and K. Griest, “Supersymmetric dark mat-
1147 ter,” *Physics Reports*, vol. 267, no. 5, pp. 195–373, 1996, ISSN: 0370-1573.
1148 DOI: [https://doi.org/10.1016/0370-1573\(95\)00058-5](https://doi.org/10.1016/0370-1573(95)00058-5). [Online].
1149 Available: <https://www.sciencedirect.com/science/article/pii/0370157395000585> (cit. on p. 7).
- 1150 [44] G. Esposito, *An introduction to quantum gravity*, 2011. arXiv: 1108.3269
1151 [hep-th] (cit. on p. 8).
- 1152 [45] G. Aad *et al.*, “Observation of a new particle in the search for the Standard
1153 Model Higgs boson with the ATLAS detector at the LHC,” *Phys. Lett. B*,
1154 vol. 716, pp. 1–29, 2012. DOI: 10.1016/j.physletb.2012.08.020. arXiv:
1155 1207.7214 [hep-ex] (cit. on p. 9).
- 1156 [46] S. Chatrchyan *et al.*, “Observation of a New Boson at a Mass of 125 GeV
1157 with the CMS Experiment at the LHC,” *Phys. Lett. B*, vol. 716, pp. 30–61,
1158 2012. DOI: 10.1016/j.physletb.2012.08.021. arXiv: 1207.7235 [hep-ex]
1159 (cit. on p. 9).
- 1160
- 1161
- 1162
- 1163

- 1164 [47] R. Shivni, *The deconstructed standard model equation*, Sep. 2023. [Online].
1165 Available: https://www.symmetrymagazine.org/article/the-deconstructed-standard-model-equation?language_content_entity=und (cit. on p. 10).
- 1167 [48] F. Gross *et al.*, “50 Years of Quantum Chromodynamics,” Dec. 2022. arXiv:
1168 2212.11107 [hep-ph] (cit. on pp. 10, 11).
- 1169 [49] Wikipedia, *Structure constants — Wikipedia, the free encyclopedia*, <http://en.wikipedia.org/w/index.php?title=Structure%20constants&oldid=1160301276>, [Online; accessed 07-October-2023], 2023 (cit. on p. 10).
- 1172 [50] K. Chetyrkin and A. Rétey, “Renormalization and running of quark mass
1173 and field in the regularization invariant and schemes at three and four loops,”
1174 *Nuclear Physics B*, vol. 583, no. 1-2, pp. 3–34, Sep. 2000. DOI: 10.1016/s0550-
1175 3213(00)00331-x. [Online]. Available: <https://doi.org/10.1016%2Fs0550-3213%2800%2900331-x> (cit. on p. 11).
- 1177 [51] S. Weinberg, “New Approach to the Renormalization Group,” *Phys. Rev. D*,
1178 vol. 8, no. 10, pp. 3497–3509, Nov. 1973. DOI: 10.1103/PhysRevD.8.3497
1179 (cit. on p. 12).
- 1180 [52] R. L. Workman *et al.*, “Review of Particle Physics,” *PTEP*, vol. 2022, p. 083C01,
1181 2022. DOI: 10.1093/ptep/ptac097 (cit. on pp. 12, 13, 15, 18).
- 1182 [53] C. G. Callan, R. F. Dashen, and D. J. Gross, “The structure of the gauge
1183 theory vacuum,” *Physics Letters B*, vol. 63, no. 3, pp. 334–340, Aug. 1976.
1184 DOI: 10.1016/0370-2693(76)90277-X (cit. on p. 12).
- 1185 [54] J. L. Rosner, “CP symmetry violation,” Sep. 2001. arXiv: hep-ph/0109240
1186 (cit. on p. 12).
- 1187 [55] R. D. Peccei, “The Strong CP problem and axions,” *Lect. Notes Phys.*, vol. 741,
1188 M. Kuster, G. Raffelt, and B. Beltran, Eds., pp. 3–17, 2008. DOI: 10.1007/
1189 978-3-540-73518-2_1. arXiv: hep-ph/0607268 (cit. on p. 12).
- 1190 [56] J. J. Lodder, “On gluon masses, color symmetry, and a possible massive ninth
1191 gluon,” Jun. 1996. arXiv: hep-ph/9606317 (cit. on p. 12).
- 1192 [57] ”. Griffiths”, *Introduction to Elementary Particles*, ”2nd”. ”Wiley-VCH”,
1193 ”2008”, pp. 280–281, ISBN: ”978-3-527-40601-2” (cit. on p. 12).

- 1194 [58] T. Luthe, A. Maier, P. Marquard, and Y. Schroder, “Complete renormalization
 1195 of QCD at five loops,” *JHEP*, vol. 03, p. 020, 2017. DOI: 10.1007/
 1196 JHEP03(2017)020. arXiv: 1701.07068 [hep-ph] (cit. on p. 12).
- 1197 [59] B. Andersson, G. Gustafson, G. Ingelman, and T. Sjöstrand, “Parton fragmentation and string dynamics,” *Phys. Rep.*, vol. 97, no. 2-3, pp. 31–145,
 1198 Jul. 1983. DOI: 10.1016/0370-1573(83)90080-7 (cit. on pp. 13, 38).
- 1200 [60] ”. Wilson and others”, ”superconducting accelerator research and development at slac”, ”*SLAC-PUB*”, vol. ”749”, ”1970” (cit. on p. 13).
- 1202 [61] R. K. Ellis, W. J. Stirling, and B. R. Webber, *QCD and Collider Physics*
 1203 (Cambridge Monographs on Particle Physics, Nuclear Physics and Cosmology). Cambridge University Press, 1996. DOI: 10.1017/CBO9780511628788
 1204 (cit. on p. 16).
- 1206 [62] U. W. Heinz, “The Strongly coupled quark-gluon plasma created at RHIC,”
 1207 *J. Phys. A*, vol. 42, D. Neilson and G. Senatore, Eds., p. 214003, 2009. DOI:
 1208 10.1088/1751-8113/42/21/214003. arXiv: 0810.5529 [nucl-th] (cit. on
 1209 p. 17).
- 1210 [63] J. Letessier and J. Rafelski, *Hadrons and Quark-Gluon Plasma*. Oxford Uni-
 1211 versity Press, 2002, ISBN: 978-1-00-929075-3, 978-0-511-53499-7, 978-1-00-929070-
 1212 8, 978-1-00-929073-9. DOI: 10.1017/9781009290753 (cit. on p. 17).
- 1213 [64] A. Maire, “Phase diagram of QCD matter : Quark-Gluon Plasma,” General
 1214 Photo, 2015. [Online]. Available: <https://cds.cern.ch/record/2025215>
 1215 (cit. on p. 17).
- 1216 [65] J. Rafelski, “Connecting QGP-Heavy Ion Physics to the Early Universe,”
 1217 *Nucl. Phys. B Proc. Suppl.*, vol. 243-244, R. Battiston and S. Bertolucci, Eds.,
 1218 pp. 155–162, 2013. DOI: 10.1016/j.nuclphysbps.2013.09.017. arXiv:
 1219 1306.2471 [astro-ph.CO] (cit. on p. 18).
- 1220 [66] E. Annala *et al.*, “Evidence for quark-matter cores in massive neutron stars,”
 1221 *Nature Phys.*, vol. 16, no. 9, pp. 907–910, 2020. DOI: 10.1038/s41567-020-
 1222 0914-9. arXiv: 1903.09121 [astro-ph.HE] (cit. on p. 18).

- 1223 [67] F.-M. Liu and S.-X. Liu, “Quark-gluon plasma formation time and direct
 1224 photons from heavy ion collisions,” *Phys. Rev. C*, vol. 89, no. 3, p. 034906,
 1225 2014. DOI: 10.1103/PhysRevC.89.034906. arXiv: 1212.6587 [nucl-th]
 1226 (cit. on p. 19).
- 1227 [68] Aug. 2021. [Online]. Available: <https://cerncourier.com/a/participants-and-spectators-at-the-heavy-ion-fireball/> (cit. on p. 21).
- 1229 [69] B. Abelev *et al.*, “Centrality determination of Pb-Pb collisions at $\sqrt{s_{NN}} =$
 1230 2.76 TeV with ALICE,” *Phys. Rev. C*, vol. 88, no. 4, p. 044909, 2013. DOI:
 1231 10.1103/PhysRevC.88.044909. arXiv: 1301.4361 [nucl-ex] (cit. on p. 22).
- 1232 [70] “Centrality determination in heavy ion collisions,” Aug. 2018 (cit. on pp. 22,
 1233 23).
- 1234 [71] M. L. Miller, K. Reygers, S. J. Sanders, and P. Steinberg, “Glauber modeling
 1235 in high energy nuclear collisions,” *Ann. Rev. Nucl. Part. Sci.*, vol. 57, pp. 205–
 1236 243, 2007. DOI: 10.1146/annurev.nucl.57.090506.123020. arXiv: nucl-
 1237 ex/0701025 (cit. on p. 22).
- 1238 [72] D. J. Gross and F. Wilczek, “Ultraviolet Behavior of Non-Abelian Gauge The-
 1239 ories,” *Phys. Rev. Lett.*, vol. 30, no. 26, pp. 1343–1346, Jun. 1973. DOI:
 1240 10.1103/PhysRevLett.30.1343 (cit. on p. 23).
- 1241 [73] H. Stoecker, “Collective flow signals the quark gluon plasma,” *Nucl. Phys. A*,
 1242 vol. 750, D. Rischke and G. Levin, Eds., pp. 121–147, 2005. DOI: 10.1016/j.
 1243 nuclphysa.2004.12.074. arXiv: nucl-th/0406018 (cit. on p. 23).
- 1244 [74] S. Cao and X.-N. Wang, “Jet quenching and medium response in high-energy
 1245 heavy-ion collisions: a review,” *Rept. Prog. Phys.*, vol. 84, no. 2, p. 024301,
 1246 2021. DOI: 10.1088/1361-6633/abc22b. arXiv: 2002.04028 [hep-ph] (cit.
 1247 on p. 24).
- 1248 [75] A. Collaboration, “ATLAS Feature: Looking inside trillion degree matter,”
 1249 General Photo, 2022. [Online]. Available: <https://cds.cern.ch/record/2809432> (cit. on p. 25).
- 1251 [76] C. Adler *et al.*, “Disappearance of back-to-back high p_T hadron correlations
 1252 in central Au+Au collisions at $\sqrt{s_{NN}} = 200\text{-GeV}$,” *Phys. Rev. Lett.*, vol. 90,
 1253 p. 082302, 2003. DOI: 10.1103/PhysRevLett.90.082302. arXiv: nucl-
 1254 ex/0210033 (cit. on pp. 25, 26).

- 1255 [77] K. Aamodt *et al.*, “Elliptic flow of charged particles in Pb-Pb collisions at 2.76
1256 TeV,” *Phys. Rev. Lett.*, vol. 105, p. 252302, 2010. DOI: 10.1103/PhysRevLett.
1257 105.252302. arXiv: 1011.3914 [nucl-ex] (cit. on pp. 26, 27).
- 1258 [78] P. Bo žek, “Splitting of proton-antiproton directed flow in relativistic heavy-
1259 ion collisions,” *Phys. Rev. C*, vol. 106, p. L061901, 6 Dec. 2022. DOI: 10.1103/
1260 PhysRevC.106.L061901. [Online]. Available: <https://link.aps.org/doi/10.1103/PhysRevC.106.L061901> (cit. on p. 27).
- 1262 [79] M. Luzum and J.-Y. Ollitrault, “Directed flow at midrapidity in heavy-ion col-
1263 lisions,” *Phys. Rev. Lett.*, vol. 106, p. 102301, 2011. DOI: 10.1103/PhysRevLett.
1264 106.102301. arXiv: 1011.6361 [nucl-ex] (cit. on p. 27).
- 1265 [80] A. M. Poskanzer and S. A. Voloshin, “Methods for analyzing anisotropic flow
1266 in relativistic nuclear collisions,” *Phys. Rev. C*, vol. 58, pp. 1671–1678, 3 Sep.
1267 1998. DOI: 10.1103/PhysRevC.58.1671. [Online]. Available: <https://link.aps.org/doi/10.1103/PhysRevC.58.1671> (cit. on p. 28).
- 1269 [81] J. Letessier and J. Rafelski, “Strangeness chemical equilibration in QGP at
1270 RHIC and CERN LHC,” *Phys. Rev. C*, vol. 75, p. 014905, 2007. DOI: 10.
1271 1103/PhysRevC.75.014905. arXiv: nucl-th/0602047 (cit. on p. 28).
- 1272 [82] I. Montvay and J. Zimanyi, “hadron chemistry in heavy ion collisions,” *Nu-
1273 clear Physics*, 1978. [Online]. Available: https://inis.iaea.org/collection/NCLCollectionStore/_Public/10/468/10468108.pdf (cit. on p. 28).
- 1275 [83] J. Cleymans *et al.*, “Statistical model predictions for particle ratios at s(NN)**(1/2)
1276 = 5.5-TeV,” *Phys. Rev. C*, vol. 74, p. 034903, 2006. DOI: 10.1103/PhysRevC.
1277 74.034903. arXiv: hep-ph/0604237 (cit. on p. 28).
- 1278 [84] A. Andronic, P. Braun-Munzinger, and J. Stachel, “Thermal hadron produc-
1279 tion in relativistic nuclear collisions,” *Acta Phys. Polon. B*, vol. 40, pp. 1005–
1280 1012, 2009. arXiv: 0901.2909 [nucl-th] (cit. on p. 28).
- 1281 [85] R. Hagedorn and J. Ranft, “Statistical thermodynamics of strong interactions
1282 at high-energies. 2. Momentum spectra of particles produced in pp-collisions,”
1283 *Nuovo Cim. Suppl.*, vol. 6, pp. 169–354, 1968 (cit. on p. 28).

- 1284 [86] F. Becattini and U. W. Heinz, “Thermal hadron production in p p and p anti-
 1285 p collisions,” *Z. Phys. C*, vol. 76, pp. 269–286, 1997, [Erratum: Z.Phys.C 76,
 1286 578 (1997)]. DOI: 10.1007/s002880050551. arXiv: hep-ph/9702274 (cit. on
 1287 p. 28).
- 1288 [87] J. Adam *et al.*, “Enhanced production of multi-strange hadrons in high-multiplicity
 1289 proton-proton collisions,” *Nature Phys.*, vol. 13, pp. 535–539, 2017. DOI: 10.
 1290 1038/nphys4111. arXiv: 1606.07424 [nucl-ex] (cit. on p. 30).
- 1291 [88] F. Becattini and J. Manninen, “Strangeness production from SPS to LHC,” *J.
 1292 Phys. G*, vol. 35, J.-e. Alam *et al.*, Eds., p. 104013, 2008. DOI: 10.1088/0954-
 1293 3899/35/10/104013. arXiv: 0805.0098 [nucl-th] (cit. on p. 29).
- 1294 [89] T. Pierog and K. Werner, “EPOS Model and Ultra High Energy Cosmic Rays,”
 1295 *Nucl. Phys. B Proc. Suppl.*, vol. 196, J.-N. Capdevielle, R. Engel, and B.
 1296 Pattison, Eds., pp. 102–105, 2009. DOI: 10.1016/j.nuclphysbps.2009.09.
 1297 017. arXiv: 0905.1198 [hep-ph] (cit. on p. 31).
- 1298 [90] C. Bierlich *et al.*, “A comprehensive guide to the physics and usage of PYTHIA
 1299 8.3,” Mar. 2022. DOI: 10.21468/SciPostPhysCodeb.8. arXiv: 2203.11601
 1300 [hep-ph] (cit. on p. 31).
- 1301 [91] S. Roesler, R. Engel, and J. Ranft, “The Monte Carlo event generator DPMJET-
 1302 III,” in *International Conference on Advanced Monte Carlo for Radiation
 1303 Physics, Particle Transport Simulation and Applications (MC 2000)*, Dec.
 1304 2000, pp. 1033–1038. DOI: 10.1007/978-3-642-18211-2_166. arXiv: hep-
 1305 ph/0012252 (cit. on p. 31).
- 1306 [92] W. Cassing and E. L. Bratkovskaya, “Parton transport and hadronization from
 1307 the dynamical quasiparticle point of view,” *Phys. Rev. C*, vol. 78, p. 034919,
 1308 2008. DOI: 10.1103/PhysRevC.78.034919. arXiv: 0808.0022 [hep-ph] (cit.
 1309 on pp. 31, 35).
- 1310 [93] W. Cassing and E. L. Bratkovskaya, “Parton-Hadron-String Dynamics: an
 1311 off-shell transport approach for relativistic energies,” *Nucl. Phys. A*, vol. 831,
 1312 pp. 215–242, 2009. DOI: 10.1016/j.nuclphysa.2009.09.007. arXiv: 0907.
 1313 5331 [nucl-th] (cit. on pp. 31, 32).

- 1314 [94] W. Cassing, “From Kadanoff-Baym dynamics to off-shell parton transport,”
 1315 *Eur. Phys. J. ST*, vol. 168, R. Alkofer, H. Gies, and B.-J. Schaefer, Eds., pp. 3–
 1316 87, 2009. DOI: 10.1140/epjst/e2009-00959-x. arXiv: 0808.0715 [nucl-th]
 1317 (cit. on p. 31).
- 1318 [95] O. Soloveva, J. Aichelin, and E. Bratkovskaya, “Transport properties and
 1319 equation-of-state of hot and dense QGP matter near the critical endpoint in
 1320 the phenomenological dynamical quasiparticle model,” *Phys. Rev. D*, vol. 105,
 1321 no. 5, p. 054011, 2022. DOI: 10.1103/PhysRevD.105.054011. arXiv: 2108.
 1322 08561 [hep-ph] (cit. on p. 32).
- 1323 [96] T. Sjostrand, “PYTHIA 5.7 and JETSET 7.4: Physics and manual,” Feb. 1994.
 1324 arXiv: hep-ph/9508391 (cit. on p. 34).
- 1325 [97] W. Ehehalt and W. Cassing, “Relativistic transport approach for nucleus nu-
 1326 cleus collisions from SIS to SPS energies,” *Nucl. Phys. A*, vol. 602, pp. 449–
 1327 486, 1996. DOI: 10.1016/0375-9474(96)00097-8 (cit. on p. 35).
- 1328 [98] Y. Nambu and G. Jona-Lasinio, “Dynamical Model of Elementary Particles
 1329 Based on an Analogy with Superconductivity. I,” *Physical Review*, vol. 122,
 1330 no. 1, pp. 345–358, Apr. 1961. DOI: 10.1103/PhysRev.122.345 (cit. on p. 36).
- 1331 [99] T. Pierog *et al.*, “Epos lhc: Test of collective hadronization with data measured
 1332 at the cern large hadron collider,” *Phys. Rev. C*, vol. 92, p. 034906, 3 Sep.
 1333 2015. DOI: 10.1103/PhysRevC.92.034906. [Online]. Available: <https://link.aps.org/doi/10.1103/PhysRevC.92.034906> (cit. on pp. 36, 37).
- 1335 [100] Z. Wolff and D. Molnar, “Self-consistent Cooper-Frye freeze-out of a viscous
 1336 fluid to particles,” *J. Phys. Conf. Ser.*, vol. 535, p. 012020, 2014. DOI: 10.
 1337 1088/1742-6596/535/1/012020. arXiv: 1407.6413 [nucl-th] (cit. on p. 36).
- 1338 [101] S. Roesler, R. Engel, and J. Ranft, “The monte carlo event generator DPMJET-
 1339 III,” in *Advanced Monte Carlo for Radiation Physics, Particle Transport Sim-
 1340 ulation and Applications*, Springer Berlin Heidelberg, 2001. arXiv: 0012252
 1341 [hep-ph] (cit. on p. 38).
- 1342 [102] A. Capella, U. Sukhatme, C.-I. Tan, and J. Tran Thanh Van, “Dual par-
 1343 ton model,” *Phys. Rept.*, vol. 236, pp. 225–329, 1994. DOI: 10.1016/0370-
 1344 1573(94)90064-7 (cit. on p. 38).